



# Coupled mechano-diffusional driving forces for fracture in electrode materials

Y.F. Gao<sup>a</sup>, M. Zhou<sup>a,b,\*</sup>

<sup>a</sup> The George W. Woodruff School of Mechanical Engineering, Georgia Institute of Technology, Atlanta, GA30332-0405, USA

<sup>b</sup> WCU Program on Multiscale Mechanical Design, School of Mechanical and Aerospace Engineering, Seoul National University, Seoul, Republic of Korea

## H I G H L I G H T S

- ▶ A theory of coupled mechano-diffusional driving forces for fracture ( $J$ -integral) is developed.
- ▶ Analysis shows that  $J$  and  $K$  are not uniquely related due to full deformation–diffusion coupling.
- ▶ Global yielding and lithiation-induced softening reduce energy release rate in thin-film Li/Si electrodes.
- ▶ Operation at higher Li concentrations mitigates fracture of thin-film Li/Si electrodes.
- ▶ A design map is developed for guiding the safe operation of thin-film Li/Si electrodes.

## A R T I C L E I N F O

### Article history:

Received 31 October 2012

Received in revised form

28 November 2012

Accepted 6 December 2012

Available online 13 December 2012

### Keywords:

Lithium ion battery

Fracture

Plasticity

Energy release rate

Stress intensity factor

silicon

## A B S T R A C T

Li/Si undergoes significant softening in the form of rapid decreases in elastic modulus and yield stress as lithium concentration increases. To investigate how this lithiation-induced softening affects the fracture behavior of electrodes, we formulate a  $J$ -integral for coupled mechanical deformation and mass diffusion processes. This measure is used to analyze mechano-diffusional driving forces for fracture through simulations using a mixed finite element framework. Calculations show that under tensile loading, Li accumulates in front of crack tips, leading to an anti-shielding effect on the energy release rate. For a pre-cracked Li/Si thin-film electrode, it is found that the driving force for fracture is significantly lower when the electrode is operated at higher Li concentrations – a result of more effective stress relaxation via global yielding. The results indicate that operation at higher concentrations is an effective means to minimize failure of thin-film Li/Si alloy electrodes. A design map for avoiding failure is developed.

© 2012 Elsevier B.V. All rights reserved.

## 1. Introduction

Electrode degradation due to internal stress build-up during cycling has been one of the key challenges for secondary battery designers. When guest atoms are inserted or extracted from the host in an electrode, the material in the electrode expands or contracts, inducing stresses that may cause material cracking [1]. This issue is especially important in alloy-based electrode materials, which are attractive because their capacities are much higher than that of graphite, but at the same time experience much higher

volume expansions. Size reduction has been proven to be an effective means to mitigate mechanical failure [2]. In particular, alloy-based electrodes made of nano-sized structures have been demonstrated to significantly improve cyclability [3–7].

Many models have been proposed to characterize the buildup and mitigation of stresses in Li-ion battery electrodes [2,8–14]. Bower et al. [15] developed a comprehensive framework and used it to analyze time-dependent plasticity in thin-film Li/Si. The effect of stress-enhanced diffusion (SED) was analyzed, revealing significant reduction in stress due to a mechanical driving force for diffusion when the deformation is in the elastic regime [16]. This enhancement effect can nevertheless be diminished or even fully reversed when the material deforms plastically [17]. Deshpande et al. [18] considered the effect of surface stresses and concluded that surface effect can reduce the tensile stresses in nano-sized electrodes, thereby improving electrode cyclability. Zhao et al.

\* Corresponding author. The George W. Woodruff School of Mechanical Engineering, Georgia Institute of Technology, Atlanta, GA30332-0405, USA. Tel.: +1 404 894 3294; fax: +1 404 894 0186.

E-mail address: [min.zhou@gatech.edu](mailto:min.zhou@gatech.edu) (M. Zhou).

[19] considered plastic deformation and showed that inelastic flow can significantly alleviate stresses in Li/Si. The mechanisms for stress reduction considered in these analyses include stress-enhanced diffusion of Li, surface-effect-induced compressive stresses, and plasticity.

Among the many candidates for next-generation negative electrode materials, silicon is considered one of the most promising because of its high capacity and low cost. Although pure silicon is brittle, both experimental and theoretical studies show that lithiated silicon can undergo significant plastic deformation [20–22]. Studies also show that such a transition from brittle to ductile is gradual, with both the elastic modulus and yield stress decreasing continuously as Li concentration increases [20,23,24]. However, how such lithiation-induced softening affects the fracture tendency of Li/Si electrodes is neither well-understood nor quantified.

The fact that lithiated Li/Si deforms plastically indicates that elastic–plastic fracture mechanics, instead of linear elastic fracture mechanics (LEFM), should be used to characterize failure. What complicates the problem is the fact that the distribution of Li, which gives rise to stresses, is in turn affected by the stress state [15,25,26]. When a crack is mechanically loaded, Li ions would accumulate in front of the crack tip, in a fashion similar to that seen hydrogen embrittlement problems [27,28]. This accumulation of Li ions at the crack tip can have profound implications on the driving forces for fracture.

Recently, Ryu et al. [11] proposed a framework for calculating the energy release rate  $J$  for cracks in Si nanowire electrodes and used the framework to study the size dependence of fracture. This theory relies on an “effective diffusivity”  $D_{eff}$  into which the effect of stress on diffusion is lumped. Such an effective diffusivity is only applicable to linear elastic problems. Specifically, when a material deforms plastically, diffusion is no longer governed by  $D_{eff}$  and the overall diffusion kinetics depends on the nature of mechanical constraints as well as other factors [17]. Even in the elastic regime, calculations based on  $D_{eff}$  can only capture stress-induced enhancement to diffusion [16] in regions far from the crack tip but cannot capture the trapping of Li ions at the crack tip [28]. To correctly account for the underlying processes responsible for fracture which include Li trapping and plasticity, a fully-coupled theory is needed to assess the energy release rate.

Here, such a fully-coupled theory is developed and used to analyze the coupled mechano-diffusional driving forces for fracture in electrode materials. The analyses take advantage of a mixed finite element framework [29,30]. We first formulate a  $J$ -integral for coupled mechanical deformation and mass diffusion processes as a measure for the driving forces for crack growth. By treating the crack tip as a separate thermodynamic system, the formulation entails detailed account of balances of mass and energy and evolution of entropy. All relevant energy forms that may contribute to fracture are explicitly tracked. It is found that the standard form of  $J$ -integral for energy release is no longer path-independent when coupled mechano-diffusion driving forces are present. Instead, an area integral similar to those in hygrothermal [31] and dynamic [32–34] problems must be included. A numerical scheme for implementing this path-independent formulation through finite element simulations is also given.

The numerical study based on the framework is carried out in a progressive manner, with increasing complexity in each step. In Section 3.1, we first consider the linear elastic case with concentration-independent properties, so that the near-tip stress fields and the energy release rate can be compared with those given by purely mechanical LEFM. It is found that stress-induced lithium redistribution significantly affects energy release, but has no effect on in-plane stress fields and hence the stress intensity factor  $K_I$ . The implication of such a dichotomy is discussed by drawing an analogy

to the difference between plane-strain and plane-stress situations in LEFM.

The next step in the analyses (Section 3.2.1) assumes a finite yield stress so that the material can deform plastically. This scenario involves elasto-plastic deformation with concentration-independent elastic properties and yield stress. The calculation focuses on a surface crack in a thin-film electrode. Depending on whether the electrode yields globally, two regimes of response can be identified. Before global yielding, the energy release rate is governed by an effective crack length which is analogous to that proposed by Irwin. After the global yielding threshold, however, it is found that plastic deformation significantly reduces the energy release rate and softer materials generally have much lower energy release rate levels.

Finally in Section 3.2.2, the effect of lithiation-induced softening on fracture tendency is added. The calculations consider deformation/diffusion coupling, plastic flow, and lithiation-induced material softening through decreases in the elastic modulus and yield stress as Li concentration increases. The analyses lead to a design map for the configuration and operation of thin-film Li–Si electrodes.

## 2. Energy release rate under full diffusion–deformation coupling

We consider the energy release rate for fracture in a solid electrode with full diffusion–deformation coupling. The material, which is composed of two chemical species: host (denoted as  $H$ ) and guest (lithium), is assumed to be highly conductive so that the whole electrode is at the same electric potential. The electrode is assumed to be fully amorphized from the beginning so that phase separation due to crystalline/amorphous transition does not need to be considered. During charge/discharge, lithium atoms diffuse, while the host atoms are assumed to undergo convection but not diffusion [29]. The movement of the host atoms therefore defines the continuum deformation  $\mathbf{x} = \mathbf{x}(\mathbf{X}, t)$ . The Eulerian concentrations of the host and lithium, namely the atomic numbers per unit current volume, are denoted by  $c^H$  and  $c^{Li}$ , respectively. Their Lagrangian counter parts  $C^H$  and  $C^{Li}$  are related to  $c^H$  and  $c^{Li}$  through  $C^H = \det(\mathbf{F})c^H$  and  $C^{Li} = \det(\mathbf{F})c^{Li}$ , where  $\mathbf{F} = \partial\mathbf{x}/\partial\mathbf{X}$  is the deformation gradient. Under the assumption of zero host diffusivity,  $C^H$  does not change with time, and a single dimensionless composition  $\xi \equiv C^{Li}/C^H$  can be used to conveniently characterize the local state of charge. This dimensionless composition  $\xi$  corresponds to the lithium number per host in the chemical formula  $\text{Li}_\xi\text{H}$ . The maximum  $\xi$  at the fully charged state is denoted as  $\xi_{\max}$ , and the state of charge (SOC) relative to this fully charged state is denoted as  $\Xi \equiv \xi/\xi_{\max}$ .

Following the standard theory of large-deformation plasticity, a Lee-type decomposition [15,35] can be performed for the deformation gradient, i.e.,

$$\mathbf{F} = \mathbf{F}^e \cdot \mathbf{F}^{SF} \cdot \mathbf{F}^p, \quad (1)$$

where  $\mathbf{F}^e$ ,  $\mathbf{F}^{SF}$  and  $\mathbf{F}^p$  are the elastic, stress-free volumetric and plastic deformation gradients, respectively [12,15]. The associated rates of deformation are

$$\left. \begin{aligned} \mathbf{D}^e &\equiv \left[ \dot{\mathbf{F}}^e (\mathbf{F}^e)^{-1} \right]_{sym}, \\ \mathbf{D}^{SF} &\equiv \left[ \mathbf{F}^e \cdot \dot{\mathbf{F}}^{SF} \cdot (\mathbf{F}^{SF})^{-1} \cdot (\mathbf{F}^e)^{-1} \right]_{sym}, \\ \mathbf{D}^p &\equiv \left[ \mathbf{F}^e \cdot \mathbf{F}^{SF} \cdot \dot{\mathbf{F}}^p \cdot (\mathbf{F}^p)^{-1} \cdot (\mathbf{F}^{SF})^{-1} \cdot (\mathbf{F}^e)^{-1} \right]_{sym}, \text{ and} \\ \mathbf{D} &= \left[ \dot{\mathbf{F}}(\mathbf{F})^{-1} \right]_{sym} = \mathbf{D}^e + \mathbf{D}^{SF} + \mathbf{D}^p. \end{aligned} \right\} \quad (2)$$

We assume the stress-free expansion due to concentration change is isotropic so that

$$\mathbf{F}^{SF} = V^{SF}(\xi) \mathbf{I} = [J^{SF}(\xi)]^{1/3} \mathbf{I}, \quad (3)$$

where  $J^{SF}(\xi) = \det(\mathbf{F}^{SF})$  measures the volume change due to changes in Li concentration.  $V^{SF} = [J^{SF}(\xi)]^{1/3}$  is the associated stretch.

The diffusion–deformation coupling comprises of two interdependent aspects. The first aspect, the effect of diffusion-induced stress (DIS), arises due to a  $C^{Li}$ -dependent term in the constitutive relationship between  $\mathbf{D}$  and  $\dot{\boldsymbol{\sigma}}$  [cf. Eqs. (A.4) and (A.5)], where  $\dot{C}^{Li}$  is the time rate of  $C^{Li}$  and  $\dot{\boldsymbol{\sigma}}$  is an objective rate (e.g., the Jaumann rate) of the Cauchy stress  $\boldsymbol{\sigma}$ . The second aspect, the effect of mechanical driving forces on diffusion, is embodied by a stress-driven term  $\mathbf{J}^{Li, mech}$  in the total Lagrangian flux  $\mathbf{J}^{Li}$  of lithium [cf. Eq. (A.17)]. These two aspects, together with the conservation laws of mass [Eq. (A.9)] and momentum [Eq. (A.7)], govern the material response in a solid electrode during charge and discharge. A brief overview of this continuum framework is given in Appendix A.

The consideration of the energy release rate ( $J$ ) for fracture is based on an account of the balance of mechanical work in a cracked body [33]. For electrodes whose response is affected by diffusion–deformation coupling, care must be taken because mechanical energy is no longer the only energy source at work. Specifically, chemical energy which drives the mixing between Li and host may also constitute a significant contribution to the overall energy balance. Such coupled driving forces for fracture in electrode materials are similar to those in hygro-thermal systems. Chen [31] proposed a generalized contour integral method to evaluate the latter. The method, however, is path-dependent and requires infinitesimal contours near the crack tip for accurate evaluation.

In this section, we use non-equilibrium thermodynamics to develop a path-independent  $J$ -integral for the coupled mechano-diffusional driving forces for fracture in electrode materials that undergo large elasto-plastic deformations. The analysis treats the crack tip as a separate thermodynamic system, therefore allowing a systematic account of the balance of mass and energy and the production of entropy. A numerical scheme for implementing this path-independent formulation in finite element simulations is also developed.

### 2.1. Energy balance and entropy production

The analysis of energy release rate under full diffusion–deformation coupling is based on accounts of energy and entropy. For any material point in the continuum body, the first law of thermodynamics [36] requires that

$$\dot{e} = \nabla_{\mathbf{x}} \cdot (\boldsymbol{\sigma}^{PK1} \cdot \mathbf{v} - \mathbf{J}^q - u^{Li} \mathbf{J}^{Li}), \quad (4)$$

where  $e$  is the internal energy per unit reference volume,  $\mathbf{v} = d\mathbf{x}/dt|_{\mathbf{x}}$  is particle velocity,  $\boldsymbol{\sigma}^{PK1} = \det(\mathbf{F}) \mathbf{F}^{-1} \cdot \boldsymbol{\sigma}$  is the first Piola–Kirchhoff stress, and  $u^{Li} \equiv \partial e / \partial C^{Li}|_{\theta}$  is the partial atomic energy of Li.  $\mathbf{J}^q$  and  $\mathbf{J}^{Li}$  are the heat flux and Li atom flux, respectively, both measured in the reference configuration. In writing Eq. (4), we have assumed that there is no external volumetric heat source. Under this condition, the 2nd law of thermodynamics can be stated as [36]

$$\left\{ \begin{array}{l} \Sigma = \dot{\eta} + \nabla_{\mathbf{x}} \cdot \mathbf{J}^{\eta} \geq 0, \text{ where} \\ \mathbf{J}^{\eta} = \frac{\mathbf{J}^q}{\theta} + \frac{(u^{Li} - \mu^{Li}) \mathbf{J}^{Li}}{\theta}. \end{array} \right. \quad (5)$$

Here,  $\eta$  and  $\mathbf{J}^{\eta}$  are the Lagrangian density and flux of entropy, respectively;  $\theta$  is temperature; and  $\Sigma$  is the rate of entropy production per unit reference volume. In this paper, isothermal conditions are assumed to prevail [i.e.,  $\theta = \theta(\mathbf{x}, t) = \text{constant}$ ], therefore

$$\Sigma = \dot{\eta} + \frac{1}{\theta} \nabla_{\mathbf{x}} \cdot [\mathbf{J}^q + (u^{Li} - \mu^{Li}) \mathbf{J}^{Li}] \geq 0. \quad (6)$$

The entropy production rate  $\Sigma$  phenomenologically characterizes the irreversible nature of the processes in the continuum. For materials that deform plastically,  $\Sigma$  can be identified as the sum of  $\Sigma^P$  (which is due to plastic flow) and  $\Sigma^{NP}$  (which is due to dissipation mechanisms other than plastic deformation, e.g. diffusion), i.e.,

$$\left\{ \begin{array}{l} \Sigma = \Sigma^P + \Sigma^{NP}, \\ \Sigma^P = \frac{\det(\mathbf{F})}{\theta} \boldsymbol{\sigma} : \mathbf{D}^P \geq 0, \text{ and} \\ \Sigma^{NP} \geq 0. \end{array} \right. \quad (7)$$

### 2.2. The crack tip subsystem

Following Moran and Shih [37,38] and Freund [39], we consider a 2-D body in the  $(\mathbf{e}_1, \mathbf{e}_2)$  plane with a crack extending along the  $\mathbf{e}_1$  direction, as illustrated in Fig. 1a. At time  $t$ , the crack has length  $l = l(t)$  in the Lagrangian configuration. The crack tip, which propagates at speed  $\dot{l}$  in the reference configuration, can be isolated using a small Lagrangian contour  $\Gamma$  which translates along with the crack tip. The nominal out-of-plane thickness (i.e., nominal thickness along  $\mathbf{e}_3$ ) of the 2-D body, also measured in the reference configuration, is denoted as  $d^{crack}$ .

Consider a larger contour  $C_0$  which is fixed with respect to the material. There is no singularity in domain A bounded by  $\Gamma$ ,  $C_0$  and the two crack surfaces  $C_-$  and  $C_+$ . In the crack-tip domain  $V_{\Gamma}$  bounded by  $\Gamma$ ,  $C_-$  and  $C_+$ , however, singularity exists. We treat this singular point in  $V_{\Gamma}$  as a stand-alone thermodynamic subsystem  $\gamma$  which can exchange mass, energy and entropy with the surrounding continuum body. The Helmholtz free energy of this

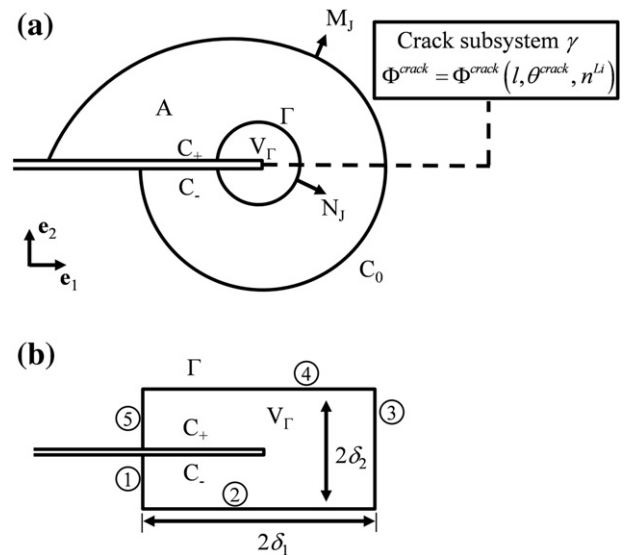


**Fig. 1.** Energy balance at the crack tip, reckoned in the Lagrangian configuration. (a) Domain A is enclosed by  $\Gamma$  and  $C = C_- + C_0 + C_+$ .  $N_{\Gamma}$  and  $M_{\Gamma}$  are unit vectors normal to  $\Gamma$  and  $C_0$ , respectively.  $V_{\Gamma}$  is the domain enclosed by  $\Gamma$ ,  $C_-$  and  $C_+$ . The infinitesimal region  $V_{\Gamma}$  exchanges energy and entropy with the crack subsystem which is characterized by its free energy  $\phi^{crack}$ . (b) A special type of contour  $\Gamma$  with rectangular shape.

subsystem per unit out-of-plane thickness  $d^{crack}$  is assumed to take the form of

$$\Phi^{crack} = \Phi^{crack}(l, \theta^{crack}, n^{Li}), \quad (8)$$

where  $\theta^{crack}$  is the temperature and  $n^{Li}$  is the amount of Li per unit  $d^{crack}$ . It turns out that Eq. (8) completely characterizes the thermodynamic properties of the crack subsystem. Specifically, the surface energy per unit crack area ( $\gamma$ ), the entropy per unit out-of-plane thickness ( $S^{crack}$ ), the chemical potential for Li ( $\mu^{Li,crack}$ ) and the internal energy per unit out-of-plane thickness ( $U^{crack}$ ) can all be uniquely determined via  $\Phi^{crack}$  as

$$\begin{cases} \gamma = \frac{1}{2} \frac{\partial \Phi^{crack}}{\partial l} \\ S^{crack} = -\frac{\partial \Phi^{crack}}{\partial \theta^{crack}}, \\ \mu^{Li,crack} = \frac{\partial \Phi^{crack}}{\partial n^{Li,crack}}, \text{ and} \\ U^{crack} = \Phi^{crack} + S^{crack} \theta^{crack}, \end{cases} \quad (9)$$

respectively. Since isothermal conditions are assumed, temperature is uniform in the continuum domain and the crack subsystem  $\gamma$  is in thermal equilibrium with its surrounding material in  $V_r$ , i.e.

$$\theta^{crack} = \theta(\mathbf{X}, t) = \text{const}. \quad (10)$$

Under this assumption, the incremental form of Eq. (8) can be simplified with the help of Eq. (9) into

$$\dot{\Phi}^{crack} = 2\gamma\dot{l} + \mu^{Li,crack}\dot{n}^{Li,crack}. \quad (11)$$

### 2.3. Energy release rate

Without loss of generality, we assume that  $\gamma$  can exchange mass, energy and entropy with the continuum body (domain A) only through  $V_r$ . In other words, we neglect any direct mass, energy and entropy exchange between  $\gamma$  and A (one possible mechanism for such direct exchange is surface adsorption on  $C_-$  and  $C_+$ ). Under this assumption, the balances of mass, energy and entropy for the combined system of  $\gamma$  and  $V_r$  (denoted as  $\gamma + V_r$ ) require that

$$\begin{cases} \text{mass:} & \dot{n}^{Li,crack} + \frac{d}{dt} \int_{V_r} C^{Li} dA_0 = - \int_{\Gamma} J_f^{Li} N_j d\Gamma_0 + \int_{\Gamma} C^{Li} \dot{l}_{1j} N_j d\Gamma_0, \\ \text{energy:} & \dot{U}^{crack} + \frac{d}{dt} \int_{V_r} e dA_0 = \int_{\Gamma} [\sigma_{ji}^{PK1} v_i - J_f^q - u^{Li} J_f^{Li} + e \dot{l}_{1j}] N_j d\Gamma_0, \\ \text{entropy:} & \dot{S}^{crack} + \frac{d}{dt} \int_{V_r} \eta dA_0 = \Sigma^{crack} + \int_{V_r} \Sigma dA_0 - \int_{\Gamma} \left( \frac{J_f^q + (u^{Li} - \mu^{Li}) J_f^{Li}}{\theta} + \eta \dot{l}_{1j} \right) N_j d\Gamma_0. \end{cases} \quad (12)$$

Here,  $\int_{V_r} (\bullet) dA_0$  stands for area integral over the 2D Lagrangian domain  $V_r$ , while  $\int_{\Gamma} (\bullet) d\Gamma_0$  stands for path integral along the 2D contour  $\Gamma$ . The area element  $dA_0$  and line segment  $d\Gamma_0$  are both measured in the reference configuration.  $\Sigma^{crack} \geq 0$  is the entropy production rate (per unit  $d^{crack}$ ), which can be due to dissipation inside  $\gamma$  or dissipation associated with interactions between  $\gamma$  and

$V_r$ . In the derivation of Eq. (12), use has been made of the Reynold transport theorem on the local forms of Eqs. (A.9), (4) and (5).

Combining the last two equations of Eq. (12) with Eq. (9) under isothermal conditions gives

$$\begin{aligned} \dot{\Phi} + \frac{d}{dt} \int_{V_r} \phi dA_0 &= \int_{\Gamma} \sigma_{ji}^{PK1} v_i N_j d\Gamma_0 + \int_{\Gamma} \phi \dot{l}_{1j} N_j d\Gamma_0 \\ &- \int_{\Gamma} \mu^{Li} J_f^{Li} \cdot \mathbf{N} d\Gamma_0 - \theta \left[ \Sigma^{crack} + \int_{V_r} \Sigma dA_0 \right], \end{aligned} \quad (13)$$

where  $\phi = \varepsilon - \eta\theta$  is the Helmholtz free energy of the continuum per unit reference volume. Again,  $\Sigma^{crack} \geq 0$  and  $\Sigma \geq 0$  here, according to the 2nd law of thermodynamics.

Equation (13) embodies the balance that accounts for the transfer and dissipation of Helmholtz free energy around the crack tip. The significance of its terms can be explained as follows. The left hand side,  $\dot{\Phi} + (d/dt) \int_{V_r} \phi dA_0$ , is the time rate of the total Helmholtz free energy in the combined system  $\gamma + V_r$ . This system comprises of everything enclosed by the moving boundary  $\Gamma$ , including the singularity point. The four terms on the right hand side are, respectively, the rates of the mechanical work done by domain A to  $\gamma + V_r$  (1st term), the free energy swept into  $\gamma + V_r$  by the moving boundary  $\Gamma$  (2nd term), the free energy conveyed into  $\gamma + V_r$  by mass flux (3rd term), and the loss of available free energy in  $\gamma + V_r$  due to irreversible dissipation (4th term). Here, the shape of  $\Gamma$  is arbitrary and, except Eq. (8), no specific assumptions on material constitutive behavior are made in the derivation of Eq. (13).

Note that Eq. (13) accounts for different dissipation mechanisms in the continuum, including inelastic flow [e.g.,  $\Sigma^P$  in Eq. (7)] and mass transport [which can be lumped into  $\Sigma^{NP}$  in Eq. (7)]. The only requirement is that the 2nd law of thermodynamics is satisfied such that  $\Sigma^{crack} \geq 0$  and  $\Sigma \geq 0$ . Now, consider the specific constitutive response described in Appendix A, in the limit that  $\Gamma$  shrinks to the crack tip. For the form of  $\phi$  given by Eqs. (A.12)–(A.15), the singularity satisfies the condition

$$\lim_{\Gamma \rightarrow 0} \left( \frac{d}{dt} \int_{V_r} \phi dA_0 \right) = 0. \quad (14)$$

This is true as long as  $\alpha < 1$  for the asymptotic behavior of  $\sigma_{ij} \sim 1/r^\alpha$  when  $r \rightarrow 0$ , where  $r$  is the radial distance measured from the crack tip. On the other hand, the form of chemical potential  $\mu^{Li}$  used in Eq. (A.13)–(A.15) ensures that  $0 \leq \xi \leq \xi_{\max}$  even when  $\sigma_m \sim 1/r^\alpha$  goes to infinity as  $r \rightarrow 0$ . The fact that  $\xi$  (and hence  $C^{Li}$ ) is continuous and bounded leads to

$$\begin{cases} \lim_{\Gamma \rightarrow 0} \left( \frac{d}{dt} \int_{V_r} C^{Li} dA_0 \right) = 0, \text{ and} \\ \lim_{\Gamma \rightarrow 0} \left( \int_{\Gamma} C^{Li} \dot{\delta}_{1j} N_j d\Gamma_0 \right) = 0. \end{cases} \quad (15)$$

Mass conservation near the crack tip [cf. Eq. (12)] when  $\Gamma \rightarrow 0$ , therefore, takes the form

$$\dot{n}^{Li, crack} = - \lim_{\Gamma \rightarrow 0} \int_{\Gamma} J_j^{Li} N_j d\Gamma_0, \quad (16)$$

i.e., Li atoms that transport into  $\gamma + V_r$  through  $\Gamma$  are predominantly stored in the crack tip subsystem  $\gamma$  if  $\Gamma \rightarrow 0$ .

Generally speaking, lithium chemical potential  $\mu^{Li}$  in  $V_r$  is position-dependent and not necessarily equal to  $\mu^{Li, crack}$  in the  $\gamma$  subsystem. When  $\mu^{Li} \neq \mu^{Li, crack}$ , the transport of Li into  $\gamma$  (at the rate of  $\dot{n}^{Li, crack}$ ) is dissipative and can be characterized by a positive-definite dissipation rate of  $\lim_{\Gamma \rightarrow 0} [\dot{n}^{Li, crack} (\mu^{Li} - \mu^{Li, crack})]$ . For simplicity, such a dissipation mechanism is not considered in this paper, i.e., it is assumed that  $\gamma$  is in chemical equilibrium with its immediate surroundings such that

$$\mu^{Li, crack} = \lim_{\Gamma \rightarrow 0} \mu^{Li}. \quad (17)$$

This assumption [Eq. (17)] and Eq. (16) immediately lead to

$$\lim_{\Gamma \rightarrow 0} \int_{\Gamma} \mu^{Li} J_j^{Li} \cdot N_j d\Gamma_0 = -\mu^{Li, crack} \dot{n}^{Li, crack}. \quad (18)$$

Combining Eqs. (11), (13), (14) and (18), therefore, yields

$$\lim_{\Gamma \rightarrow 0} \int_{\Gamma} \left[ \sigma_{ji}^{PK1} v_i + \phi \dot{\delta}_{1j} \right] N_j d\Gamma_0 = 2\gamma \dot{l} + \theta \left[ \Sigma^{crack} + \lim_{\Gamma \rightarrow 0} \int_{V_r} \Sigma dA_0 \right]. \quad (19)$$

The left hand side of Eq. (19) is the time rate at which energy is imparted into the crack tip region during crack growth. Under the conditions of local steady state,  $v_i \sim -\dot{l}(\partial u_i / \partial X_1)$ . The driving force for crack growth, namely energy provided per unit new crack area created, is therefore given by

$$\begin{aligned} J &\equiv \lim_{\Gamma \rightarrow 0} \frac{1}{\dot{l}} \int_{\Gamma} \left[ \sigma_{ji}^{PK1} v_i + \phi \dot{\delta}_{1j} \right] N_j d\Gamma_0 \\ &= \lim_{\Gamma \rightarrow 0} \int_{\Gamma} \left[ \phi \dot{\delta}_{1j} - \sigma_{ji}^{PK1} \frac{\partial u_i}{\partial X_1} \right] N_j d\Gamma_0. \end{aligned} \quad (20)$$

The right hand side of Eq. (19), on the other hand, comprises two parts. The first part  $2\gamma \dot{l}$  corresponds to the increase of free energy in the subsystem  $\gamma$ , while the second part  $\theta [\Sigma^{crack} + \lim_{\Gamma \rightarrow 0} \int_{V_r} \Sigma dA_0]$  characterizes the free energy loss due to dissipation. As for any irreversible processes, this dissipation is generally history-dependent, in the sense that the combined resistance

$$J_{CR} \equiv 2\gamma + \lim_{\Gamma \rightarrow 0} \frac{\theta \left[ \Sigma^{crack} + \lim_{\Gamma \rightarrow 0} \int_{V_r} \Sigma dA_0 \right]}{\dot{l}} \quad (21)$$

depends on the history of crack growth even for the same thermodynamic state ( $l, g^{crack}, n^{Li}$ ) of the crack tip subsystem  $\gamma$ . For simplicity, the standard assumption of fracture mechanics that  $J_{CR} = J_{CR}(l)$  is used here, with the understanding that  $J_{CR}$  may also

depend on the state of charge (i.e., Li concentration) in the electrode. Under this assumption, the critical condition for isothermal quasi-static crack growth accounting for deformation–diffusion coupling can be stated as

$$J = J_{CR} \geq 2\gamma. \quad (22)$$

Equation (22) is the Griffith condition for fracture growth when diffusion–deformation two-way coupling is present. It should be noted that as a fracture mechanics criterion, the Griffith condition generally does not apply to fatigue crack growth and the failure of secondary battery electrodes can occur under static or cyclic loads (charge–discharge). However, for an electrode to last, it has to survive the first few cycles of loading during which fracture is governed by Eq. (22). As will be shown in the numerical analysis in Section 3, even this requirement alone puts significant constraints on the design of battery electrodes. We, therefore, use Eq. (22) as the criterion for battery failure in this paper, and leave the discussion of cyclic fatigue to future studies. It should be also noted that even for situations in which fatigue is important, analyses such as the Paris-law generally require the calculation of fracture driving force (in the form of  $K_I$  or  $J$ ). The fully-coupled theory in this paper can, therefore, also be regarded as an essential part of future models for cyclic failure in battery electrodes.

#### 2.4. Path-independent integral for energy release rate

The specific form of Eq. (20) is general but inconvenient for the numerical evaluation of energy release rate because the integral

$$J^*(\Gamma) \equiv \int_{\Gamma} \left[ \phi \dot{\delta}_{1j} - \sigma_{ji}^{PK1} \frac{\partial u_i}{\partial X_1} \right] N_j d\Gamma_0 \quad (23)$$

is path-dependent for coupled diffusion/deformation problems. Indeed, for any continuum domain  $\Omega$  bound by  $\partial\Omega$ , it can be proven that (see Appendix B)

$$J^*(\partial\Omega) = - \int_{\partial\Omega} w^p \delta_{1j} N_j d\Gamma_0 + \int_{\Omega} \mu^{Li} \frac{\partial C^{Li}}{\partial X_1} dA_0, \quad (24)$$

where the plastic potential  $w^p$  is defined as

$$\begin{cases} w^p \equiv \int_0^t (V^{SF})^2 \sigma_{jk}^{PK2} \dot{E}_{jk}^p dt, \text{ where} \\ E_{jk}^p \equiv \frac{1}{2} (F_{jj}^p F_{jk}^p - \delta_{jk}) \end{cases} \quad (25)$$

Here,  $\sigma^{PK2} = \det(\mathbf{F}) \mathbf{F}^{-1} \cdot \boldsymbol{\sigma} \cdot \mathbf{F}^{-T}$  is the 2nd Piola–Kirchhoff stress, and  $\mathbf{E}^p$  is the Lagrangian strain of plastic deformation. Subtracting Eq. (24) from Eq. (23) leads to the path-independent integral form of

$$\begin{aligned} J(\Gamma) &\equiv \int_{\Gamma} \left[ \phi \dot{\delta}_{1j} - \sigma_{ji}^{PK1} (\partial u_i / \partial X_1) \right] N_j d\Gamma_0 \\ &\quad - \left( \int_{V_r} \mu^{Li} \frac{\partial C^{Li}}{\partial X_1} dA_0 - \int_{\Gamma} w^p \delta_{1j} N_j d\Gamma_0 \right). \end{aligned} \quad (26)$$

The integral  $J(\Gamma)$  is path-independent, in the sense that  $J(\partial\Omega) = 0$  for the boundary  $\partial\Omega$  of any continuum domain  $\Omega$ . On the other hand, contour  $\Gamma$  in Eq. (20) can be of arbitrary shape as long as its size is infinitesimal. To establish a link between Eqs. (20) and (26), consider the special type of  $\Gamma$  shown in Fig. 1(b). As pointed out by



Freund [39], if the rectangular contour is shrunk onto the crack tip by first letting  $\delta_2 \rightarrow 0$  and then  $\delta_1 \rightarrow 0$ , one has

$$J = \lim_{\delta_1 \rightarrow 0} \lim_{\delta_2 \rightarrow 0} \int_{\Gamma} \left[ \phi \delta_{1j} - \sigma_{ji}^{PK1} \frac{\partial u_i}{\partial X_1} \right] N_j d\Gamma_0. \quad (27)$$

Such rectangular contours are especially convenient because horizontal segments 2 and 4 do not contribute to the integral  $\int_{1-2-3-4-5} w^p \delta_{1j} N_j d\Gamma_0$  [cf. Fig. 2(b)]. Even if  $w^p$  is singular at the crack tip, the plasticity term in Eq. (26) still vanishes as long as appropriate limiting process is considered, i.e.

$$\lim_{\delta_1 \rightarrow 0} \lim_{\delta_2 \rightarrow 0} \int_{\Gamma} w^p \delta_{1j} N_j d\Gamma_0 = 0. \quad (28)$$

On the other hand, for domain  $V_{\Gamma}$  bound by  $\Gamma$  [cf. Fig. 2(b)],  $\int_{V_{\Gamma}} \mu^{Li} (\partial C^{Li} / \partial X_1) dA_0$  can be evaluated and goes to 0 when  $\delta_2 \rightarrow 0$  and  $\delta_1 \rightarrow 0$ , i.e.,

$$\lim_{\delta_1 \rightarrow 0} \lim_{\delta_2 \rightarrow 0} \int_{V_{\Gamma}} \mu^{Li} (\partial C^{Li} / \partial X_1) dA_0 = 0. \quad (29)$$

Combining Eqs. (26)–(29), therefore, leads to the path-independent  $J$ -integral for coupled mechano-diffusional driving forces in the form of

$$J = J(\Gamma) = \int_{\Gamma} \left[ \left( \phi + w^p \right) \delta_{1j} - \sigma_{ji}^{PK1} \frac{\partial u_i}{\partial X_1} \right] N_j d\Gamma_0 - \int_{V_{\Gamma}} \mu^{Li} \frac{\partial C^{Li}}{\partial X_1} dA_0, \quad (30)$$

where  $\Gamma$  is arbitrary. With Eqs. (A.11)–(A.13) and some algebra, Eq. (30) can be recast into

$$J = J(\Gamma) = \int_{\Gamma} \left[ \left( w + w^p \right) \delta_{1j} - \sigma_{ji}^{PK1} (\partial u_i / \partial X_1) \right] N_j d\Gamma_0 - \int_{V_{\Gamma}} \left( \frac{\partial w}{\partial C^{Li}} \Big|_{\mathbf{F}^e, \theta} - \det(\mathbf{F}^e) \Omega^{Li(SF)} \sigma_m \right) \frac{\partial C^{Li}}{\partial X_1} dA_0, \quad (31)$$

where  $w$  is the elastic strain energy given by Eq. (A.12).

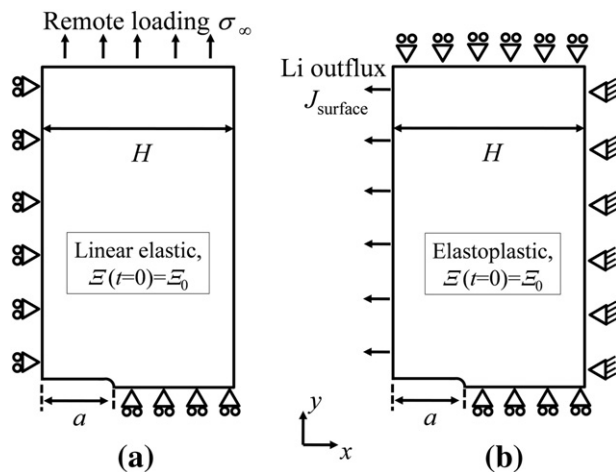


**Fig. 2.** (a) A highly-simplified plane-strain system with a center crack in a 2D media, loaded by a remote stress. This configuration will be used to analyze the effect of diffusion/deformation coupling in the LEFM regime. (b) A thin-film electrode with periodic surface pre-cracks, initial homogeneous Li concentration  $\varepsilon_0$ , and zero initial stress undergoing discharge at a constant surface outflux. The pre-crack is modeled as a notch with a small but finite tip radius of  $\rho \ll a$  for numerical stability.

Equations (30) and (31) will be used to evaluate energy release rates from numerical results given by finite element simulations. The main advantage of this path-independent form lies in the fact that  $\Gamma$  can be far away from the crack tip region where the numerical evaluation of  $\phi$ ,  $w^p$ ,  $\partial u_i / \partial X_1$  and  $\sigma_{ji}^{PK1}$  is usually more challenging. We implemented Eqs. (30) and (31) using the energy domain integral method originally proposed by Shih et al. [40]. The details of this numerical implementation can be found in Appendix C.

### 3. Results and discussions

The analyses carried out concern the energy release rate for stationary cracks. Specifically, a large-deformation, mixed finite element framework of the rate form is used to analyze the coupling between diffusion and stress development [29,30]. Based on numerical solutions obtained, the energy release rate is calculated using the path-independent form in Section 2. The issues of focus are

- 1) How does the mechanical driving force for diffusion affect crack-tip fields and energy release rate?
- 2) How does plasticity affect the energy release rate in the presence of diffusion/deformation coupling?
- 3) How does lithiation-induced softening affect fracture and, in turn, battery design?

To address the first issue, we consider a highly-simplified plane-strain system with a center crack in a 2D media (Fig. 2a). Lithiation-induced softening is not considered in this case and the material is assumed to be perfectly elastic. When the crack is loaded by a remotely applied stress  $\sigma_{\infty}$ , the effect of diffusion/deformation coupling can be analyzed, especially in terms of crack-tip fields and energy release rate.

Based on the insights gained from the above LEFM problem, a more realistic case with material inelasticity will be considered to address the second and the third issues. Specifically, a thin-film electrode with surface cracks during delithiation will be considered (cf. Fig. 2b). Analyses in this regard will be carried out in two steps. The first step involves constant mechanical properties that are independent of Li concentration (Section 3.2.1). After that, the implications of lithiation-induced softening will be analyzed (Section 3.2.2).

Depending on the design and material, stresses in an electrode may arise via three mechanisms: (1) Li concentration inhomogeneity due to finite diffusivity, (2) lattice mismatch at phase boundaries, and (3) constraining by external agencies such as substrate or current collector. In order to focus on the effect of deformation/diffusion coupling and lithiation-induced softening on the fracture driving forces, we only consider the third mechanism (mechanical constraint) in this paper. To this end, we assume that the initial material (Li/Si in this paper) is fully amorphized and that the characteristic loading time  $T_0$  is much longer than the characteristic diffusion time  $\tau^{Li} \approx H^2 / D_0^{Li}$  so that the stresses in the electrode are entirely due to external loading (for Fig. 2a) or mechanical constraint (for Fig. 2b). The insight thus obtained can be easily extended to situations with  $\tau^{Li} \sim T_0$ , which will not be the focus of this paper.

#### 3.1. Linear elastic case

We first consider the linear elastic situation such that the yield stress  $\sigma_Y$  is infinite and Young's modulus  $E$  and Poisson ratio  $\nu$  are  $\varepsilon$ -independent. The geometry of the stress-controlled configuration (cf. Fig. 2a) used here can be characterized by a single parameter  $a$  which measures the crack length, as long as  $H \gg a$ . The

**Table 1**  
Concentration-independent material parameters for Li<sub>x</sub>Si used in the LEFM analysis.

Parameter	Symbol	Typical value	Reference/definition
Partial atomic volume of Li	$\Omega^{\text{Li}}(\text{SF})$	14.2 Å <sup>3</sup>	[1]
Si concentration in fully-discharged state	$C_0^{\text{Si}}$	49.3 atoms nm <sup>-3</sup>	[41]
Young's modulus	$E$	80 GPa	[42]
Diffusivity	$D_0^{\text{Li}}$	10 <sup>-11</sup> cm <sup>2</sup> s <sup>-1</sup>	[43–47]
Poisson ratio	$\nu$	0.22	[11]
Maximum charging limit of Li <sub>x</sub> Si	$\xi_{\text{max}}$	3.75	[48]
Chemical-to-mechanical partial atomic volume	$\tilde{Q}^{\text{CM}}$	0.7	$\Omega^{\text{Li}}(\text{SF}) C^{\text{Si}}$
Mechanical-to-chemical dimensionless partial atomic volume	$\tilde{Q}^{\text{MC}}$	274	$\Omega^{\text{Li}}(\text{SF}) E / k\theta$

pre-crack is modeled as a notch with a small but finite tip radius of  $\rho \ll a$  for numerical stability. Starting from a stress-free state with homogeneous initial SOC of  $\Xi_0$ , the system is loaded by a remote stress of  $\sigma_\infty = (t/T_0)E$  with  $\tau^{\text{Li}} \ll T_0$ . Under the condition of  $\tau^{\text{Li}} \ll T_0$ , the concentration and stress fields, hence the fracture driving forces, do not depend on  $D_0^{\text{Li}}$  explicitly. Our task is to analyze the effect of mechanical driving force for diffusion on crack-tip fields and the energy release rate.

Four dimensionless parameters can be identified here: the charging limit  $\xi_{\text{max}}$ , the Poisson's ratio  $\nu$ , and dimensionless partial atomic volumes  $\tilde{Q}^{\text{CM}} \equiv \Omega^{\text{Li}}(\text{SF}) C^{\text{Si}}$  and  $\tilde{Q}^{\text{MC}} \equiv \Omega^{\text{Li}}(\text{SF}) E / k_B \theta$ . The meaning of  $\tilde{Q}^{\text{CM}}$  is straightforward: it characterizes the volume expansion ratio when Li concentration changes. Specifically, the ratio between the volume at lithiated state Li<sub>x</sub>H and the volume at fully-delithiated state Li<sub>0</sub>H is  $J^{\text{SF}}(\xi) = 1 + \xi \tilde{Q}^{\text{CM}}$ .  $\tilde{Q}^{\text{CM}}$ , therefore, determines the effect of chemical diffusion to mechanical deformation (Chemical-to-Mechanical, CM) when composition changes. To illustrate the significance of  $\tilde{Q}^{\text{MC}}$ , on the other hand, we consider the dimensionless chemical potential  $\mu^{\text{Li}}/k_B \theta$  which can be easily shown from Eqs. (A.13)–(A.15) to be

$$\frac{\mu^{\text{Li}}}{k_B \theta} = \left( \frac{\mu_*^{\text{Li}}}{k_B \theta} + \ln \frac{\Xi}{1 - \Xi} \right) - \tilde{Q}^{\text{MC}} \frac{\sigma_m}{E}. \quad (32)$$

The first term of Eq. (32) is the chemical contribution to  $\mu^{\text{Li}}/k_B \theta$ , the second term is due to mechanical stresses. Since  $\sigma_m/E$  is proportional to elastic strain  $\epsilon^e$  [cf. Eq. (A.1) and (A.2)], one can immediately conclude from Fick's law [Eq. (A.10)] that  $\tilde{Q}^{\text{MC}}$  is the

parameter which controls the mechanical driving force to chemical diffusion (Mechanical-to-Chemical, MC). Specifically, if  $\tilde{Q}^{\text{MC}} = 0$  there would be no stress effect on  $J^{\text{Li}}$ .

The role of  $\tilde{Q}^{\text{MC}}$  has been widely studied, especially in the context of thermally-induced fracture. The significance of  $\tilde{Q}^{\text{MC}}$  and associated effect on fracture, however, are still not well-understood. To see how  $\tilde{Q}^{\text{MC}}$  affects crack-tip fields and energy release rate, we used the typical room-temperature ( $\theta = 300$  K) values of material parameters for Li<sub>x</sub>Si ( $H = \text{Si}$  for Li<sub>x</sub>H). The discussions compare two scenarios: one with  $\tilde{Q}^{\text{MC}} = \tilde{Q}_{\text{LiSi}}^{\text{MC}}$  as listed in Table 1, and the other with  $\tilde{Q}^{\text{MC}} = 0$ .

### 3.1.1. In-plane stresses and stress intensity factor

Fig. 3a shows the redistribution of Li concentration  $\Xi = \xi/\xi_{\text{max}}$  when an initially homogeneous electrode (with  $a = 500$  nm and  $\Xi_0 = 0.4$ ) is loaded by a remote stress of  $\sigma_\infty = 0.005E$ , under the condition of  $\tilde{Q}^{\text{MC}} = \tilde{Q}_{\text{LiSi}}^{\text{MC}}$ . The spatial coordinates are normalized by the crack length  $a$ . It can be seen that  $\Xi$  deviates from the average value  $\bar{\Xi} = \Xi_0$  such that  $\Delta \Xi \equiv \Xi - \Xi_0 > 0$  in front of the crack tip. This redistribution, driven by the crack-tip hydrostatic stress  $\sigma_m$ , in turn relaxes  $\sigma_m$  (Fig. 3b), as shown by the much lower  $\sigma_m$  levels for the fully-coupled case ( $\tilde{Q}^{\text{MC}} = \tilde{Q}_{\text{LiSi}}^{\text{MC}}$ ) than the levels for the purely mechanical case ( $\tilde{Q}^{\text{MC}} = 0$ ).

Given the dependence of  $\sigma_m$  on  $\tilde{Q}^{\text{MC}}$ , one may conjecture that Li redistribution lowers all components of crack-tip stresses. Quite counter-intuitively, this is not the case. As shown in Fig. 4(a), the in-plane stress components ( $\sigma_{xx}$  and  $\sigma_{yy}$ ) are both independent of  $\tilde{Q}^{\text{MC}}$ . The relaxation of  $\sigma_m$  is entirely due to the change in  $\sigma_{zz}$ . Indeed, when  $\tilde{Q}^{\text{MC}} = 0$  the problem reduces to an elementary plane-strain elasticity problem with  $\sigma_{zz} = \nu(\sigma_{xx} + \sigma_{yy}) > 0$ . On the other hand for  $\tilde{Q}^{\text{MC}} = \tilde{Q}_{\text{LiSi}}^{\text{MC}}$ ,  $\sigma_{zz} < 0$  [cf. Fig. 4(b)]. Such a tensile to compressive change of  $\sigma_{zz}$  significantly increases the crack-tip von Mises stress  $\sigma_{\text{mises}}$  [compare Fig. 4(c) and (d)]. The consequence of this increase of  $\sigma_{\text{mises}}$  will be discussed further later (cf. Fig. 8).

In terms of stress intensity factor  $K_I$ , how does the coupled case here differ from the pure linear elastic case in without chemical transport of Li? This issue warrants a careful examination. If we follow the classic linear elastic fracture mechanics (LEFM) definition, the single parameter  $K_I$  that determines the in-plane stress fields near the crack tip is evaluated through

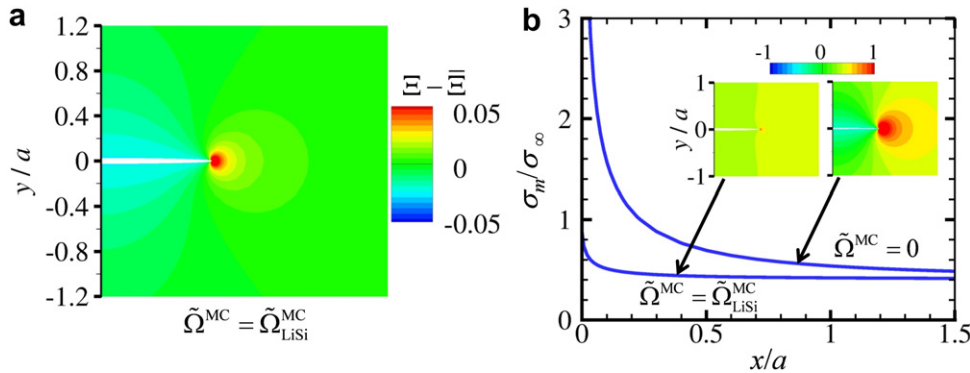


**Fig. 3.** Distributions of Li concentration and hydrostatic stress near the crack tip under a remote stress of  $\sigma_\infty = 0.005E$ . (a) deviation of concentration from its spatial average when  $\tilde{Q}^{\text{MC}} = \tilde{Q}_{\text{LiSi}}^{\text{MC}}$ ; (b) normalized hydrostatic stress  $\sigma_m/\sigma_\infty$  along the  $y = 0$  line for the fully-coupled ( $\tilde{Q}^{\text{MC}} = \tilde{Q}_{\text{LiSi}}^{\text{MC}}$ ) and the purely mechanical ( $\tilde{Q}^{\text{MC}} = 0$ ) cases. The inset in (b) shows the corresponding  $\sigma_m/\sigma_\infty$  contours. The length of the center-crack is  $a = 500$  nm and the initial SOC is  $\Xi_0 = \bar{\Xi} = 0.4$ . All spatial dimensions are normalized by crack length  $a$ .

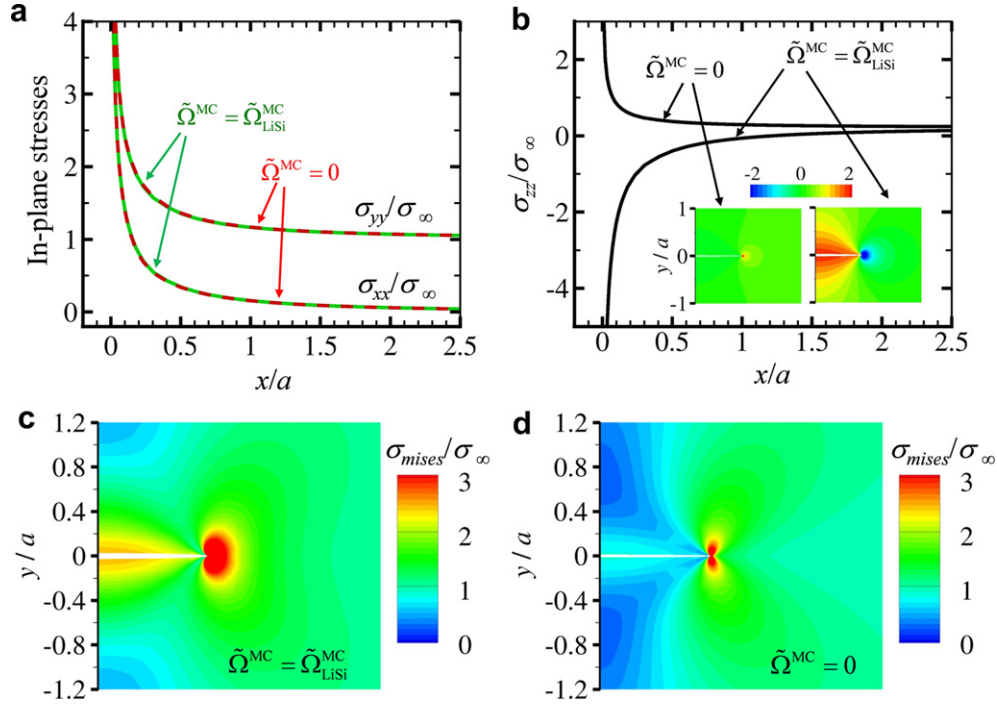


**Fig. 4.** Distributions of  $\sigma_{xx}$ ,  $\sigma_{yy}$ ,  $\sigma_{zz}$  and the von Mises effective stress  $\sigma_{mises}$  normalized by the remote stress  $\sigma_{\infty} = 0.005E$ . (a–b) Normalized in-plane stresses (a) and out-of-plane stress (b) along  $y = 0$ . (c–d) Normalized von Mises stress for fully-coupled (c) and purely mechanical (d) cases. The length of the center-crack is 500 nm and the initial SOC is  $\Xi_0 = \bar{\Xi} = 0.4$ . All the spatial dimensions are normalized by the crack length  $a$ .

$$\lim_{r \rightarrow 0} \sigma_{ij} = \frac{K_I}{\sqrt{2\pi r}} f_{ij}(\theta), \quad (i, j = 1, 2), \quad (33)$$

where  $(r, \theta)$  are the polar coordinates with origin at the crack tip. For both plane-strain and plane-stress conditions, Eq. (33) has the same form of  $f_{ij}(\theta)$ . Effect of out-of-plane constraint kicks in only through out-of-plane stress: for plane-strain,  $\sigma_{zz} = \nu(\sigma_{xx} + \sigma_{yy})$ ; for plane-stress  $\sigma_{zz} = 0$ .

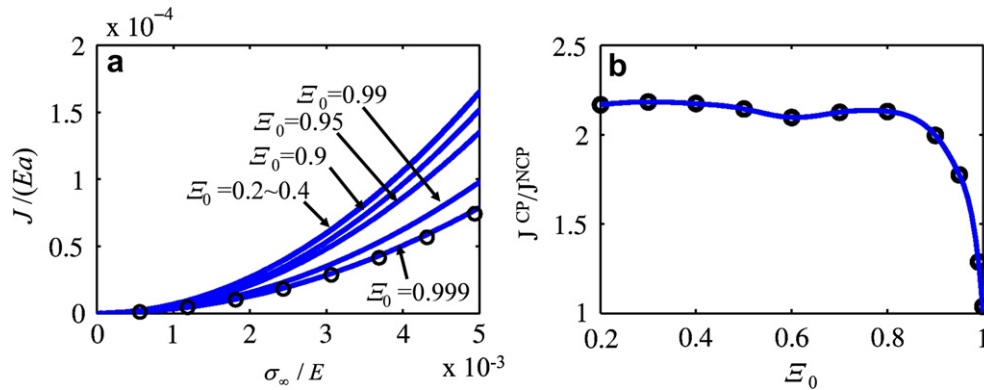
Although the stress states in Fig. 4 are computed under plane-strain conditions, the relationship of  $\sigma_{zz} = \nu(\sigma_{xx} + \sigma_{yy})$  is no-longer valid. Instead,  $\sigma_{zz} < 0$  for  $\tilde{Q}^{MC} = \tilde{Q}_{LiSi}^{MC}$ , as seen in Fig. 4b. Still, the results in Fig. 4a indicate that the in-plane stresses are independent of  $\tilde{Q}^{MC}$ . In other words, as long as the material is elastic and sufficient time is given to allow diffusion to occur (i.e.  $T_0 \gg \tau^{Li}$ ), the in-plane stresses can always be characterized by Eq. (33) even though stresses affect Li redistribution. The outcome is

that  $K_I$  is independent of the accumulation of Li at the crack tip. Consequently,  $K_I$  is incapable of capturing the full effect of diffusion–deformation coupling on fracture.

### 3.1.2. Energy release rate

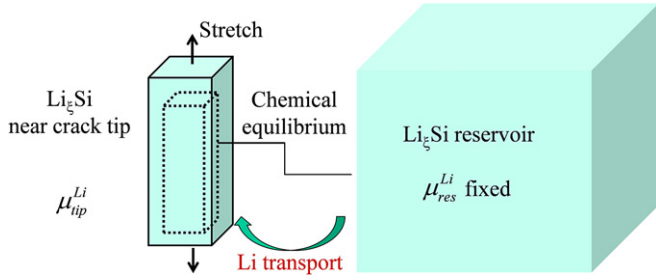
Similar findings on  $K_I$  have been made for hydrogen embrittlement of metals [27] and transformation toughening of ceramic materials [49], in the sense that the in-plane stresses are independent of dilatational eigen-strains near the stationary crack tip. This conclusion on in-plane stresses can also be proved analytically using the linear elastic compatibility conditions (which will not be elaborated here). However, previous studies have not clarified if the energy release rate, a more universal parameter for fracture analysis, changes as Li redistributes. We provide an analysis in this regard.

Fig. 5a shows the calculated  $J$  values for the range of initial concentration of  $0.2 < \Xi_0 < 0.999$ . The circular symbols denote the non-coupled energy release rate  $J^{NCP} \equiv J(\tilde{Q}^{MC} = 0)$  and the solid



**Fig. 5.** Path-independent  $J$  integral for a stationary crack in Fig. 2a using Eq. (31). (a) Energy release rate for the fully-coupled case  $J^{CP} \equiv J(\tilde{Q}^{MC} = \tilde{Q}_{LiSi}^{MC})$  as a function of remote stress for different levels of initial concentration  $\Xi_0$ , the circular symbols denote  $J^{NCP} \equiv J(\tilde{Q}^{MC} = 0)$  as the baseline for comparison. (b) Dependence of  $J^{CP}$  on initial concentration when  $K_I$  (thus  $J^{NCP}$ ) is fixed at a value that corresponds to  $a = 500$  nm and  $\sigma_{\infty} = 0.005E$ .





**Fig. 6.** Illustration of the negative effective Poisson's ratio effect. When material near the crack tip is subject to uniaxial tensile stresses, Li transported from a reservoir may overcome the elastic Poisson's effect and induce an overall expansion in the transverse directions. The cuboid with dotted boundary denotes the initial configuration of the isolated near-tip system before stretching, and the cuboid with solid boundary represent its stretched counterpart.

lines represent the fully-coupled values of  $J^{CP} \equiv J(\tilde{Q}^{MC} = \tilde{Q}_{LiSi}^{MC})$ . For  $\tilde{Q}^{MC} = 0$ ,  $J^{NCP}$  coincides with the purely mechanical LEFM result of  $J^{NCP}/(aE) = \pi(1 - \nu^2)(\sigma_\infty/E)^2$ . For  $\tilde{Q}^{MC} = \tilde{Q}_{LiSi}^{MC}$ , two observations can be made. First,  $J^{CP}$  depends on  $\Xi_0$ ; second,  $J^{CP} \geq J^{NCP}$ . Specifically, for all initial concentrations  $J^{CP}$  is always higher than  $J^{NCP}$ , except for  $\Xi_0 = 0.999$  when the two are essentially equal. This trend is more clearly seen in Fig. 5b, which shows  $J^{CP}/J^{NCP}$  as a function of  $\Xi_0$  (crack length of 500 nm and remote load  $\sigma_\infty = 0.005E$ ).

The  $\Xi_0$ -dependence of  $J^{CP}$  is due to the fact that Li content  $\Xi$  cannot exceed 1, as embodied by the fact that  $\mu_{Li}/k_B\theta \rightarrow \infty$  when  $\Xi \rightarrow 1$  [cf. Eq. (32)]. If the initial content  $\Xi_0$  is close to 1, redistribution of Li cannot happen and  $J^{CP}$  approaches  $J^{NCP}$ . The plateau for  $\Xi_0 < 0.8$  [cf. Fig. 3b], on the other hand, is due to the fact that the relaxation of  $\sigma_m$  is nearly complete such that changes in  $\Xi_0$  in the range of  $0.2 < \Xi_0 < 0.8$  bear no significant influence on  $J^{CP}$ .

The finding that  $J^{CP}/J^{NCP} \geq 1$  appears counterintuitive at the first glance: since Li redistribution is a stress relaxation mechanism, why would this redistribution cause the energy release rate to increase? It turns out that this anomaly can be associated with a negative effective Poisson's ratio effect near the crack tip. If we conceptually isolate the LiSi material near the crack tip, the bulk of LiSi far from the crack can be regarded as a reservoir with fixed Li chemical potential  $\mu_{res}^{Li}$  [Fig. 6]. Consider a uniaxial stretch applied to the near-tip material. During the stretch,  $\mu_{tip}^{Li}$  decreases as the hydrostatic stress becomes tensile. The associated chemical potential difference  $\mu_{tip}^{Li} - \mu_{res}^{Li} < 0$  drives Li from the reservoir into the crack tip. If the amount of Li so transported is large enough, the associated lithiation-induced volume change may overcome the elastic Poisson effect and lead to transverse expansion. The outcome is effectively a negative Poisson's ratio – tensile loading causes lateral dimensions to increase. This is exactly what happens here for LiSi.

To quantify this effect, we consider the limiting case with  $D_0^{Li} = \infty$ ,  $\tilde{Q}^{MC} = \infty$  and  $\xi_{max} = \infty$ . Under this condition, the chemical potential in the entire material is always in equilibrium and the mechanical contribution to diffusion  $-\tilde{Q}^{MC}(\sigma_m/E)$  dominates the chemical contribution  $\mu_{*}^{Li}/(k_B\theta) + \ln[\Xi/(1 - \Xi)]$  [cf. Eq. (32)]. Consequently,  $\sigma_m$  in the near-tip region is pinned at the same level as that in the remote regions.

For  $\tilde{Q}^{MC} = 0$ , the elastic response of the material is characterized by bulk modulus  $K$  and shear modulus  $G$ . For  $\tilde{Q}^{MC} = \infty$ , on the other hand, the overall deformation is governed by effective moduli  $G^{eff} = G$ ,  $K^{eff} = 0$ , and  $\nu^{eff} = -1$ , reflecting the fact that near-tip  $\sigma_m$  is pinned at the remote level.

Now that  $K_I$  is independent of  $\tilde{Q}^{MC}$  [Discussions in 3.1.1], the introduction of  $G^{eff}$  and  $K^{eff}$  allows  $J(\tilde{Q}^{MC} = \infty)$  to be calculated from  $K_I$  using the classic LEFM relation. Specifically,

$$J(\tilde{Q}^{MC} = \infty) = \lim_{K^{eff} \rightarrow 0} \frac{1 - (\nu^{eff})^2}{E^{eff}} K_I^2 = \frac{K_I^2}{G^{eff}} = \frac{K_I^2}{G}. \quad (34)$$

In contrast, the energy release rate for the purely mechanical case is

$$J^{NCP} = J(\tilde{Q}^{MC} = 0) = \frac{1 - \nu^2}{E} K_I^2 = \frac{1 - \nu}{2G} K_I^2. \quad (35)$$

We therefore have shown that

$$\frac{J(\tilde{Q}^{MC} = \infty)}{J(\tilde{Q}^{MC} = 0)} = \frac{2}{1 - \nu}. \quad (36)$$

Indeed, for  $\nu = 0.22$  the ratio given by Eq. (36) is 2.56, which is fairly close to the plateau value ( $\approx 2.2$ ) of  $J^{CP}/J^{NCP}$  in Fig. 5b. The difference is due to the fact that the ideal case of  $\tilde{Q}^{MC} = \infty$  [Eq. (36)] overestimates the relaxation of  $\sigma_m$  compared with the realistic case of  $\tilde{Q}^{MC} = \tilde{Q}_{LiSi}^{MC}$  [Fig. 5b].

From an energetic point of view,  $J^{CP} > J^{NCP}$  embodies the fact that the redistribution of Li provides another source of energy for the fracture driving force besides the mechanical fields. Two complementary processes make this additional source of energy available for fracture. The first is energy storage. For  $\tilde{Q}^{MC} \neq 0$ , the external agency ( $\sigma_\infty$  here) must provide extra work compared with the case with  $\tilde{Q}^{MC} = 0$  in order to induce the same remote fields. This extra work is stored as latent energy in the form of inhomogeneous Li concentration. The second mechanism is energy retrieval. Through the agency of composition-change-induced stresses, the latent energy is converted back into mechanical energy, thereby increasing the fracture driving force.

The storage process is controlled by  $\tilde{Q}^{MC}$  and the retrieval process is controlled by  $\tilde{Q}^{CM}$ . If either  $\tilde{Q}^{MC}$  or  $\tilde{Q}^{CM}$  is zero, the coupling is severed and the energy release rate reduces to the purely mechanical level. On the other hand, the analysis in Eqs. (34)–(36) provides an upper bound for the change of energy release rate due to this storage–retrieval mechanism. This limit is reached when the hydrostatic stress field is completely relaxed (to the remote level) so that full redistribution of Li has occurred. This upper bound is universal or the same for all cases regardless of material properties and loading, as long as the material response is elastic and the loading is slow.

It should be noted that the anti-shielding effect of  $J$  due to deformation–diffusion coupling (i.e., the fact that  $J^{CP} > J^{NCP}$ ) in this paper is evaluated for the steady-state of Li distribution such that  $T_0 \gg \tau^{Li}$ . Under this condition, stresses arise solely because of external constraint [Fig. 2b] or mechanical loading [Fig. 2a]. As pointed out earlier, in general stresses may also develop during charge/discharge due to concentration inhomogeneity when  $\tau^{Li} \sim T_0$ , as seen in free-standing amorphous LiSi particles or NWs [16,19,50,51]. For such situations with transient effect, deformation–diffusion full coupling would manifest itself in two aspects. First, accumulation of Li near the crack tip, again, leads to an anti-shielding effect on  $J$  which increases the magnitude of the energy release rate. Second, remote concentrations and stresses far from the crack are governed by an effective diffusivity  $D_{eff}$  [11,16]. This  $D_{eff}$  leads to a stress-enhanced-diffusion (SED) effect that

lowers the remote stresses [16] and hence  $J$ . In other words, the first effect increases  $J$  while the second effect decreases  $J$ . The final outcome is the combined effect of the two. Depending on the ratio of  $a/H$ , the characteristic time scales for the two effects can be different. This transient situation of  $\tau^{Li} \sim T_0$  is not the focus of this paper. Instead, configurations shown in Fig. 2 with  $T_0 \gg \tau^{Li}$  are considered in order to isolate the effect of Li accumulation near the crack tip (the first effect). The insight thus obtained can be easily combined with the effect of SED for far fields and thereby extended to situations with  $\tau^{Li} \sim T_0$ .

### 3.1.3. Remarks on $K_I$ -based and $J$ -based fracture approaches

We have shown earlier that  $K_I$  is independent of  $\tilde{Q}^{MC}$ , i.e.  $K_I$  is unaffected by the deformation/diffusion coupling in the long-term limit (i.e.  $T_0 \gg \tau^{Li}$ ). In contrast, Fig. 5 and Eqs. (34)–(36) show clearly that the coupled energy release rate does depend on  $\tilde{Q}^{MC}$ . Even when the conditions of plane strain are maintained, the relationship between  $J$  and  $K_I$  is no longer unique, in the sense that the coupled energy release depends on  $\tilde{Q}^{MC}$ ,  $\tilde{Q}^{CM}$  and  $\Xi_0$ . Given this dichotomy, we ponder the question of which criterion,  $K_I = K_{Ic}$  or  $J = J_{CR}$ , is more appropriate.

To answer this question, we first note that a similar dichotomy exists in classic fracture mechanics in that the relationship between  $J$  and  $K_I$  is not always unique there either. Specifically, under the same in-plane loading,  $J^{NCP} = (1 - \nu^2)K_I^2/E$  for plane-strain and  $J^{NCP} = K_I^2/E$  for plane-stress. This difference arises due to the difference in the out-of-plane constraint and, hence, crack tip stress triaxiality. Here, however, the situation is more complicated because the crack-tip stress triaxiality is not only determined by out-of-plane constraint but also by the redistribution of Li. Depending on the values of  $\tilde{Q}^{MC}$ ,  $\tilde{Q}^{CM}$  and  $\Xi_0$ ,  $\sigma_{zz}$  may assume any value between  $\nu(\sigma_{xx} + \sigma_{yy})$  and  $-(\sigma_{xx} + \sigma_{yy})$ , and  $J$  may be of any value between  $(1 - \nu^2)K_I^2/E$  [for  $\tilde{Q}^{MC} = 0$ ] and  $K_I^2/G = 2(1 + \nu)K_I^2/E$  [for  $\tilde{Q}^{MC} = \infty$ ], even under the same plane-strain conditions.

In the pure mechanical case, the fracture criterion can be stated as

$$\left. \begin{aligned} K(d^{crack}) &= K_{critical}(d^{crack}), \text{ or } \\ J(d^{crack}) &= J_{CR}(d^{crack}). \end{aligned} \right\} \quad (37)$$

The effect of crack-tip load triaxiality can be lumped into the thickness-dependence of fracture toughness  $K_{critical}(d^{crack})$  which is higher than the plane strain fracture toughness  $K_{Ic}$  and lower than the plane stress fracture toughness  $K_c$  such that  $K_{Ic} \leq K_{critical}(d^{crack}) \leq K_c$ . This handling allows the stress intensity factor  $K_I$  calculated solely from in-plane stresses, which do not depend on out-of-plane constraints, to be compared with the thickness-dependent fracture toughness  $K_{critical}(d^{crack})$  to determine the onset of fracture. As a conservative measure, the plane-strain fracture toughness  $K_{Ic}$  is most often used. A similar treatment is reflected in the  $J$ -integral based fracture criterion above in that both  $J$  and  $J_{CR}$  are thickness-dependent.

Similarly, it is also possible to state the fracture criterion for electrode materials which deforms only elastically and experience diffusion/deformation coupling as

$$\left. \begin{aligned} K(d^{crack}) &= K_{critical}(d^{crack}, \Xi_0), \text{ or } \\ J(d^{crack}, \Xi_0) &= J_{CR}(d^{crack}, \Xi_0), \end{aligned} \right\} \quad (38)$$

as long as both sides of these relations are specific to the same thickness and, in addition, the right hand sides are also specific to the initial state of charge  $\Xi_0$ . At this stage, it is unclear under what conditions the critical value functions  $K_{critical}(d^{crack}, \Xi_0)$  and  $J_{CR}(d^{crack}, \Xi_0)$  would assume their minima or most conservative values. These failure envelopes separating the safe and unsafe regions in the  $(d^{crack}, \Xi_0)$  space can only be determined by experiments.

As a concluding remark to this section, it should be noted that the results in Figs. (3)–(5) are based on the highly-idealized assumption that the material is linear elastic. Understandably, the behavior of real Li/Si, which is capable of deforming plastically, is different. The results in this section may be more applicable to cathode materials such as LiFePO<sub>4</sub> which is generally quite brittle. When significant (large-scale) plasticity is involved, the  $K$ -based criterion [the first of Eq. (38)] should not be used and the  $J$ -based criterion [the second of Eq. (38)] is the only sensible approach. Nevertheless, the analysis in this section yields insight into the behavior of alloy-based electrode materials. This discussion lays the foundation for further discussions accounting the effect of plasticity and lithiation-induced softening in the following sections.

### 3.2. Elasto-plastic case

We now turn our attention to the situation when the electrode material deforms plastically, especially when plastic deformation is large enough to render the LEFM approach using  $K$  invalid. To this end, we first consider a simplified case such that the yield stress  $\sigma_Y$  is assumed to be independent of  $\Xi_0$  (Section 3.2.1). For this purpose, we assume the same material properties and dimensionless parameters as listed in Table 1, with only one extra dimensionless number  $\bar{\sigma}_Y \equiv \sigma_Y/E \ll 1$  which quantifies concentration-independent yield stress  $\sigma_Y$ . The case with concentration-dependent  $\sigma_Y$  and elastic moduli will be considered in Section 3.2.2.

When the material deforms plastically, the stress-controlled configuration [Fig. 2(a)] used to facilitate comparison with pure mechanical LEFM solutions is no longer appropriate because any remote stress  $\sigma_\infty$  exceeding  $\sigma_Y$  would lead to large-scale plastic deformation. In this section, we therefore use the configuration shown in Fig. 2b which involves a thin-film electrode with initial thickness  $H$  and SOC  $\Xi_0$  under galvanostatic discharging. Again, the pre-defect is a surface crack with length  $a$  and a small but finite crack-tip radius of  $\rho \ll a$ . The initial stress-free state (with SOC of  $\Xi_0$ ) is taken to be the Lagrangian configuration in which the energy release rate is calculated via Eq. (31). A surface outflux of  $J_{surf}$  is specified to simulate galvanostatic discharging such that the average SOC  $\bar{\Xi}$  in the film decreases with time  $t$  according to  $\bar{\Xi}(t) = \Xi_0 - t/T_0$  for  $t < \Xi_0/T_0$ , where  $T_0 = (1 \text{ hour})/(C - \text{rate})$  is the nominal discharge time. The nominal thickness  $H_0$  is the thickness of the film in the fully discharged (i.e.,  $\Xi = 0$  throughout the electrode) state. It is related to the initial thickness  $H$  via  $H \approx J^{SF}(\Xi_0)H_0$ . The approximation is associated with elastic strains and therefore is very reasonable. Unless indicated otherwise,  $H_0$  is used because it is more convenient and almost exclusively used in the literature [20,52–54].

For the calculation in this section, a typical film thickness of  $H_0 = 200 \text{ nm}$  and nominal discharging time of  $T_0 = 50 \text{ h}$  are considered. These values are such that  $T_0 \gg \tau^{Li}$  and are in the range of available experimental data. In addition,  $a/H = a/J^{SF}(\Xi_0)H_0 \leq 1/4$ , so that the film/substrate interface does not significantly affect crack-tip fields.

#### 3.2.1. Effect of global yielding on energy release rate

For galvanostatic discharging, the dimensionless discharge level  $\Delta\bar{\Xi} \equiv \Xi_0 - \bar{\Xi}(t) = t/T_0$  can be used to conveniently characterize the

amount of Li extracted during the process. When  $T_0 \gg \tau^{Li}$ , all stresses are due to constraint at the film-substrate interface, and the bi-axial stress state far from the crack can be written as

$$\begin{cases} \sigma_{xx} = \sigma_{yy} = \frac{1}{3} \frac{E}{1-\nu} \frac{J^{SF}(\Delta\bar{\varepsilon})}{J^{SF}(\bar{\varepsilon}_0)}, & \text{for } \Delta\bar{\varepsilon} \leq \Delta\bar{\varepsilon}_Y, \\ \sigma_{xx} = \sigma_{yy} = \sigma_Y, & \text{for } \Delta\bar{\varepsilon} > \Delta\bar{\varepsilon}_Y, \end{cases} \quad (39)$$

where  $\Delta\bar{\varepsilon}_Y$  is the discharge level at which  $\sigma_{xx}$  and  $\sigma_{yy}$  reach  $\sigma_Y$  so that the film begins to yield globally.  $\Delta\bar{\varepsilon}_Y$  is approximately independent of  $\tilde{Q}^{MC}$  so long as  $T_0 \gg \tau^{Li}$ , because  $\tilde{Q}^{MC}$  only affects the Li distribution near the crack and has no bearings on stresses far away from the crack ( $y \gg H$ ) where  $\bar{\varepsilon} = \bar{\varepsilon}_0 - \Delta\bar{\varepsilon}_Y$  is homogeneous.

Fig. 7 shows the distribution of effective plastic strain  $\varepsilon_{eff}^p \equiv \int_0^t \sqrt{(2/3) \mathbf{D}^p : \mathbf{D}^p} dt$  for a film with  $\bar{\sigma}_Y = 0.01$ ,  $H_0 = 200$  nm,  $a = 50$  nm and  $\bar{\varepsilon}_0 = 0.5$ , at  $\Delta\bar{\varepsilon} = \Delta\bar{\varepsilon}_Y$  as specified by Eq. (39). The plastic zone indeed extends through the thickness (horizontal) of the film for both  $\tilde{Q}^{MC} = \tilde{Q}_{LiSi}^{MC}$  and  $\tilde{Q}^{MC} = 0$ , confirming the onset of full-scale yielding. The remote regions show slightly later yielding for  $\tilde{Q}^{MC} = \tilde{Q}_{LiSi}^{MC}$  than for  $\tilde{Q}^{MC} = 0$ , mainly because of the finite dimension in the  $y$ -direction. This slight difference does not affect the main conclusions to be drawn. On the other hand, the plastic strain near the crack is higher for  $\tilde{Q}^{MC} = \tilde{Q}_{LiSi}^{MC}$  than for  $\tilde{Q}^{MC} = 0$ , in consistency with the previous finding that Li redistribution increases the crack-tip von Mises stress [cf. Fig. 4c and d]. This promotion of plastic deformation, together with the redistribution of Li, is also responsible for the observation that the crack opening is wider for  $\tilde{Q}^{MC} = \tilde{Q}_{LiSi}^{MC}$  than for  $\tilde{Q}^{MC} = 0$  [see Fig. 8a and b].

The redistribution of Li and resultant relaxation of  $\sigma_m$  at  $\Delta\bar{\varepsilon}_Y$  are shown in Fig. 8. Although significant plastic strains are involved, the redistribution of Li [Fig. 8c] is rather similar to that in the fully elastic case [Fig. 3a]. Again, this redistribution causes  $\sigma_m$  to relax [Fig. 8a and b]. In contrast to what is seen previously, the in-plane stresses are no longer independent of  $\tilde{Q}^{MC}$ . This difference indicates that  $J$  is the only sensible parameter for characterizing the fracture behavior. It turns out that the path-independent form of  $J$  in Eq. (31)

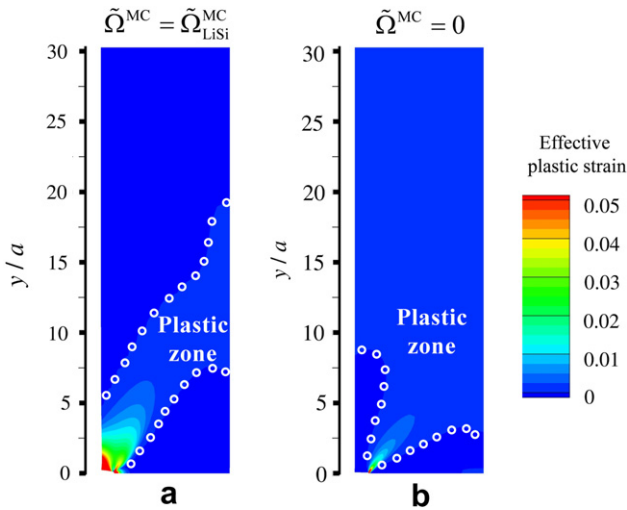


Fig. 7. Effective plastic strain  $\varepsilon_{eff}^p$  for a stationary crack with  $a = 50$  nm in a film with nominal thickness  $H_0 = 200$  nm and initial concentration of  $\bar{\varepsilon}_0 = 0.5$ , when the discharge reaches a level  $\Delta\bar{\varepsilon}_Y$  such that the film begins to yield globally with  $\bar{\sigma}_Y = 0.01$ . (a)  $\varepsilon_{eff}^p$  for fully-coupled case  $\tilde{Q}^{MC} = \tilde{Q}_{LiSi}^{MC}$ ; (b)  $\varepsilon_{eff}^p$  with  $\tilde{Q}^{MC} = 0$ .

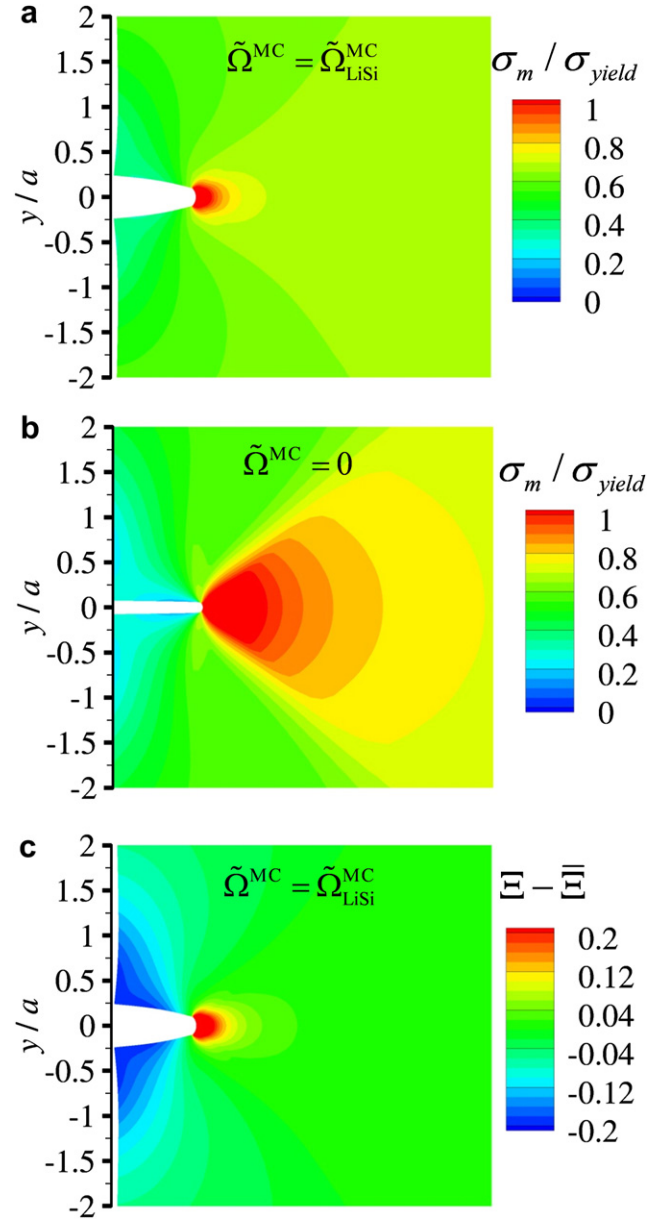
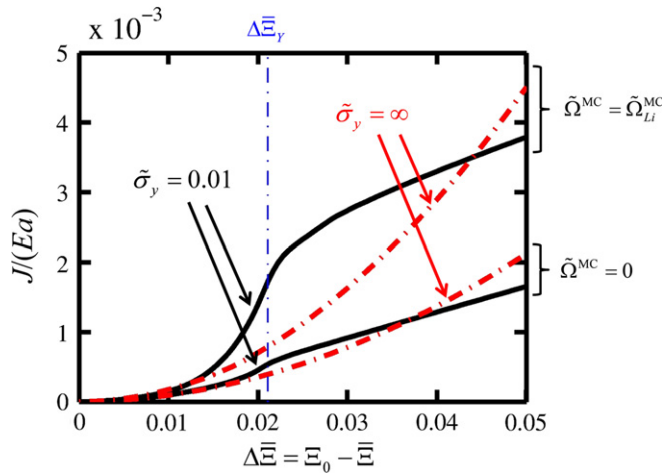


Fig. 8. Distributions of Li concentration and hydrostatic stress for a stationary crack with  $a = 50$  nm in a film with nominal thickness  $H_0 = 200$  nm and initial concentration  $\bar{\varepsilon}_0 = 0.5$ . The condition shown corresponds to onset of global yielding at  $\Delta\bar{\varepsilon} = \Delta\bar{\varepsilon}_Y$  with  $\bar{\sigma}_Y = 0.01$ . (a) hydrostatic stress normalized by yield stress for  $\tilde{Q}^{MC} = \tilde{Q}_{LiSi}^{MC}$ , (b) hydrostatic stress normalized by yield stress for  $\tilde{Q}^{MC} = 0$ , and (c) deviation of Li concentration from its average value  $\bar{\varepsilon} = \bar{\varepsilon}_0 - \Delta\bar{\varepsilon}_Y$  for  $\tilde{Q}^{MC} = \tilde{Q}_{LiSi}^{MC}$ .

is highly robust numerically, with less than 0.5% difference between  $J$  calculated from difference contours even when  $\Delta\bar{\varepsilon}$  reaches  $\Delta\bar{\varepsilon}_Y$ . A brief discussion on the numerical stability and errors associated with this method can be found in Appendix D.

Fig. 9 shows the evolution of  $J$  [normalized by  $(Ea)$ ] for  $\bar{\sigma}_Y = 0.01$  (solid black lines). Both  $J^{CP} = J(\tilde{Q}^{MC} = \tilde{Q}_{LiSi}^{MC})$  and  $J^{NCP} = J(\tilde{Q}^{MC} = 0)$  are plotted, with the corresponding curves for the purely elastic cases (red dashed lines) given for comparison. Clearly, plasticity significantly affects the energy release rate (both  $J^{CP}$  and  $J^{NCP}$ ), except for the very initial stages of discharge ( $\Delta\bar{\varepsilon} < 0.01$ ) when the plastic zone is small enough so that LEFM provides a good approximation.





**Fig. 9.** Evolution of energy release rate  $J$  for a stationary surface crack with  $a = 50$  nm in a film with nominal thickness  $H_0 = 200$  nm and initial concentration  $\bar{E}_0 = 0.5$ . Solid black lines indicate normalized values of  $J^{\text{CP}} = J(\bar{Q}^{\text{MC}} = \bar{Q}_{\text{LiSi}}^{\text{MC}})$  and  $J^{\text{NCP}} = J(\bar{Q}^{\text{MC}} = 0)$  for  $\bar{\sigma}_Y = 0.01$ . Dashed red lines show the corresponding  $J^{\text{CP}}$  and  $J^{\text{NCP}}$  values for the corresponding elastic cases. (For interpretation of the references to colour in this figure legend, the reader is referred to the web version of this article.)

As  $\Delta\bar{E}$  increases, both  $J^{\text{CP}}$  and  $J^{\text{NCP}}$  begin to deviate from their LEFM values. The most striking feature is the sudden slope changes in the  $J - \Delta\bar{E}$  curves (for both fully-coupled case of  $\bar{Q}^{\text{MC}} = \bar{Q}_{\text{LiSi}}^{\text{MC}}$  and purely mechanical case of  $\bar{Q}^{\text{MC}} = 0$ ) when  $\Delta\bar{E}$  reaches the global yielding threshold  $\Delta\bar{E}_Y$  [cf. Fig. 7]. Before  $\Delta\bar{E}_Y$ , plastic zone size  $r_Y$  is small relative to the system dimension, and the effective  $K_I$  and  $J$  can be estimated using Irwin's effective crack length  $a_{\text{eff}} = a + r_Y$  [55]. Beyond  $\Delta\bar{E} = \Delta\bar{E}_Y$ , however, the film yields globally and Irwin's assumption no longer applies. Instead, plasticity in regions far away from the crack tip becomes important. This prevents the remote stresses from increasing further and leads to much flatter  $J^{\text{CP}}$  and  $J^{\text{NCP}}$  curves. Such global yielding is important because it significantly reduces the energy release rates, thereby lowering the fracture tendency.

The shapes of the  $J - \Delta\bar{E}$  curves in Fig. 9 are consistent with that was found by Aoki et al. [56] who calculated the energy release rate for a stationary crack in a thermally-loaded plate. What they studied corresponds to the special situation with  $\bar{Q}^{\text{CM}} > 0$  and  $\bar{Q}^{\text{MC}} = 0$ . Our calculation confirms that the overall characteristics of the  $J - \Delta\bar{E}$  curve, especially the existence of inflection points, remain even for fully-coupled case with  $\bar{Q}^{\text{MC}} \neq 0$ . More importantly, Fig. 9 indicates that  $J^{\text{CP}}/J^{\text{NCP}} > 1$  even when the combined effect of plasticity and diffusion/deformation coupling is considered, although the upper bound given by the linear elastic solution [Eqs. (34)–(36)] can no longer be used directly.

Fig. 10 shows the dependence of  $J$  on  $\bar{\sigma}_Y$  for the fully-coupled case of  $\bar{Q}^{\text{MC}} = \bar{Q}_{\text{Li}}^{\text{MC}}$ . For both  $\bar{\sigma}_Y = 0.005$  and  $\bar{\sigma}_Y = 0.01$ , an inflection point is seen in the  $J - \Delta\bar{E}$  relation. The location of the inflection point for each case corresponds to its global-yielding threshold  $\Delta\bar{E}_Y$ . Overall, the reduction in  $\bar{\sigma}_Y$  lowers the fracture tendency by lowering  $J$  [e.g.  $J(\bar{\sigma}_Y = 0.005) < J(\bar{\sigma}_Y = 0.01) < J_{\text{elastic}}$  for  $\Delta\bar{E} > 0.05$ ], except for early stages before global yielding occurs so that the development of  $J$  is approximately governed by the effective crack length  $a_{\text{eff}} \geq a$ . In terms of elastic modulus, note that  $J$  is normalized by  $Ea$  so a reduction in  $E$  would also lead to a reduction in the fracture driving forces.

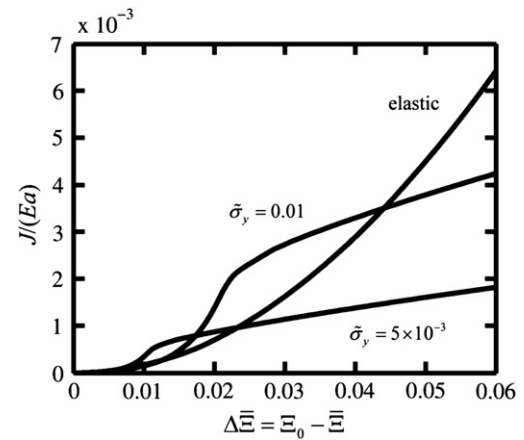


**Fig. 10.** Dependence of energy release on yield stress  $\bar{\sigma}_Y$ . The length of the surface crack is  $a = 50$  nm and the nominal film thickness is  $H_0 = 200$  nm. The initial concentration is  $\bar{E}_0 = 0.5$ . Full deformation–diffusion coupling ( $\bar{Q}^{\text{MC}} = \bar{Q}_{\text{LiSi}}^{\text{MC}}$ ) is considered.

The discharge level  $\Delta\bar{E}_{\text{CR}}$  when critical condition  $J = J_{\text{CR}}$  is reached determines the maximum extractable amount of Li without electrode failure. Designs and cycling regimens that maximize  $\Delta\bar{E}_{\text{CR}}$  would increase the utilizable capacity of the electrode without jeopardizing its cyclability. For the same  $J_{\text{CR}}$  and  $a$ , Fig. 10 shows that choosing materials with smaller  $E$  and  $\bar{\sigma}_Y$  (hence  $\sigma_Y$ ) is an effective way to avoid fracture.

### 3.2.2. Effect of lithiation-induced softening

What we learned from Fig. 10 can be important for alloy-based electrode materials, because the elastic moduli and yield stress of such materials show significant dependence on Li concentration. If we manage to find a composition window  $\bar{E} \in (\bar{E}_0 - \Delta\bar{E}_{\text{CR}}, \bar{E}_0)$  for which the combination of elastic modulus and yield stresses minimizes  $J$ , we can operate the battery in such a window to maximize the operational capacity  $\Delta\bar{E}_{\text{CR}}$ .

To find such a window for Li/Si, we now put all the insights learned thus far together and assess the combined effect of diffusion/deformation coupling, inelasticity, and lithiation-induced softening on fracturing driving force. To this end, calculations involving composition-dependent bulk modulus  $K = (12.46\xi + 65.44)/(1 + \xi)$  GPa, shear modulus  $G = (7.63\xi + 35.51)/(1 + \xi)$  GPa [23], and yield stress  $\sigma_Y = (1.75 + 0.167\xi)/(1 + \xi)$  GPa, are conducted. The variation of yield stress with concentration represents a simple interpolation between  $\sigma_Y = 1.75$  GPa at  $\xi = 0$  and  $\sigma_Y = 0.5$  GPa at  $\xi = \xi_{\text{max}}$  [57,58] using the rule of mixture. Although it is likely that  $J_{\text{CR}}$  for Li/Si is composition-dependent, we adopt a constant value of  $J_{\text{CR}} = 3$  J/m<sup>2</sup> due to lack of experimental data. This critical value is estimated using the toughness for pure silicon which is typically between 2.5–4.3 J/m<sup>2</sup> [59].

Since the mechanical properties here are concentration-dependent, dimensionless parameters  $\bar{Q}^{\text{MC}}$  and  $\bar{\sigma}_Y$  are no longer convenient, and all quantities will be stated in their respective physical units. The system configuration and discharge rate are the same as those in Section 3.2.1 [Fig. 2b], which is relevant for thin-film electrodes under galvanostatic discharge.

Fig. 11 shows the dependence of  $J$  development on initial concentration  $\bar{E}_0$ , for a film with nominal thickness of  $H_0 = 200$  nm and pre-crack length of  $a = 20$  nm. For each  $J - \Delta\bar{E}$  curve, the critical discharge level  $\Delta\bar{E}_{\text{CR}}$  at which  $J = J_{\text{CR}}$  is marked. Two scenarios can be identified. For lower  $\bar{E}_0$  [e.g.  $\bar{E}_0 < 0.6$ ] the



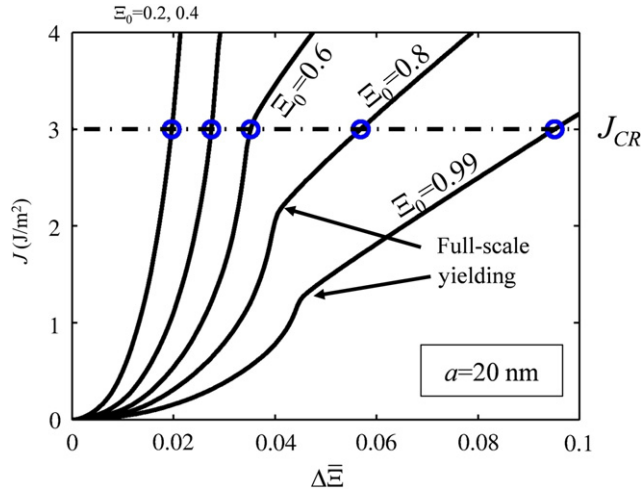


**Fig. 11.** Dependence of energy release rate on discharge level  $\Delta\bar{E}$  and initial concentration  $\bar{E}_0$  for a crack length of 20 nm. Full deformation–diffusion coupling is considered.

energy release rate reaches its critical value before the onset of full-scale yielding. For higher  $\bar{E}_0$  [e.g.  $\bar{E}_0 \geq 0.8$ ], on the other hand, the material is softer and the inflection point  $\Delta\bar{E}_Y$  is reached before fracture.

In the first scenario, fracture is essentially governed by Irwin's effective crack length. Under this condition, the  $\Delta\bar{E}_{CR} - \bar{E}_0$  dependency is mainly due to lithiation-induced elastic softening (i.e. reduction of elastic moduli as Li concentration increases). Specifically, since  $J$  is approximately proportional to the Young's modulus [note that  $J$  is normalized by  $(Ea)$  in Fig. 10], the fracture driving force is lower when the operation window is chosen at higher concentrations. In the second scenario, relaxation due to global yielding comes into play, leading to much wider windows of  $\bar{E} \in (\bar{E}_0 - \Delta\bar{E}_{CR}, \bar{E}_0)$  than that in the first scenario. The increase in  $\Delta\bar{E}_{CR}$  due to global yielding is much more significant compared with that due to elastic softening. For all cases, the maximum allowed operational capacity  $\Delta\bar{E}_{CR}$  is always higher when  $\bar{E}_0$  is higher, as a combined consequence of the lithiation-induced softening of  $E$  and  $\sigma_Y$ .

We conclude our discussion with a design map [Fig. 12] which shows the maximum utilizable amount of Li (as measured by

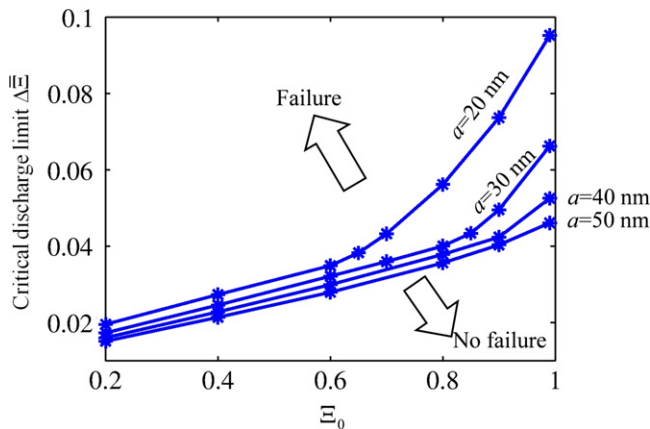


**Fig. 12.** Design map showing the maximum extractable amount of lithium  $\Delta\bar{E}$  without crack growth as a function of initial SOC  $\bar{E}_0$  for different pre-crack sizes. Full deformation–diffusion coupling is considered.

$\Delta\bar{E}$ ) as a function of  $\bar{E}_0$  when pre-cracks with different sizes are present. Again,  $\bar{E} \in (\bar{E}_0 - \Delta\bar{E}_{CR}, \bar{E}_0)$  is the safe window in which the electrode can be operated without fracture. For each pre-crack length  $a$ , the corresponding  $\Delta\bar{E}_{CR} - \bar{E}_0$  curve delineates the boundary between the unsafe region (upper left) and the safe region (bottom right). In real thin-film electrodes, the smoothness of electrode surfaces is always limited by the manufacturing and operating conditions, and the existence of surface defects is inevitable. Fig. 12 indicates that for the same operational capacity ( $\Delta\bar{E}$ ), a thin-film electrode is always more defect-tolerant when the charging/discharging regimen is designed such that the battery operates at higher concentration windows of  $\bar{E} \in (\bar{E}_0 - \Delta\bar{E}_{CR}, \bar{E}_0)$ .

As a final remark, it should be noted that  $\Delta\bar{E}_{CR}$  in Figs. 11 and 12 is calculated based on the assumption of a constant  $J_{CR}$ . For real alloy-based electrode materials, it is very likely that  $J_{CR}$  is concentration-dependent. Taking conventional engineering material as reference, the general trend for fracture toughness is that  $K_{IC}$  is higher for materials with lower  $\sigma_Y$ . If this trend is also true for Li/Si,  $J_{CR}$  would be higher at higher Li concentrations, a condition that would further reinforce the conclusion that operation at higher concentration is an effective means to mitigate failure of thin-film Li/Si electrodes. Such an analysis with composition-dependent  $J_{CR}$ , however, requires detailed experimental measurements and is not attempted in this paper.

It should also be noted that the analysis here is based on a stress-free initial condition which does not consider residue stresses from prior lithiation processes. Such a simplification, however, does not affect the primary conclusions, especially the conclusion that operation windows at higher concentrations enhance battery cyclability.

#### 4. Conclusions

A fully-coupled finite deformation theory for analyzing the coupled mechano-diffusional driving forces for fracture in electrode materials is developed. The formulation of  $J$ -integral treats the crack tip as a separate thermodynamic system and entails detailed account of balances of mass and energy and evolution of entropy. It is found that the standard form of  $J$ -integral for energy release rate is no longer path-independent when coupled mechano-diffusion driving forces are present. Instead, an area integral must be included to maintain path-independency.

A numerical scheme for implementing this path-independent formulation through mixed finite element simulations is given. This numerical scheme is found to be highly robust, even under conditions of global yielding.

Under loading, lithium accumulates at tips, leading to relaxation of hydrostatic stress. This process does not affect in-plane stress fields or the stress intensity factor as long as the material is linear elastic and sufficient time is given for diffusion to occur (i.e.  $T_0 \gg \tau^{Li}$ ). In contrast, the deformation-diffusion coupling increases the energy release rate (driving force for fracture). This anti-shielding effect on  $J$  can be understood through a negative effective Poisson's ratio effect. Specifically, the anti-shielding effect embodies the fact that the redistribution of Li provides another source of energy for the fracture besides the mechanical fields. Two complementary mechanisms make this additional source of energy available. These two mechanisms are controlled by two partial atomic volumes. The first is the chemical-to-mechanical  $\bar{Q}^{CM}$ , which controls storage. The second is the mechanical-to-chemical  $\bar{Q}^{MC}$ , which controls retrieval.

For electrode materials, energy release rate  $J$  and stress intensity factor  $K$  are not uniquely related. Under conditions of

significant plasticity,  $K$  cannot be used and  $J$  is the only sensible choice for characterizing fracture. Before global yielding, fracture is governed by Irwin's effective crack length; after global yielding, plastic deformation in regions far from the crack significantly reduces  $J$  and, hence, the likelihood of fracture. Global yielding marks an inflection point in the energy release rate-discharge level curve. In general, the driving force for fracture in thin-film electrodes can be lowered by operating at higher Li concentrations. A design map is developed to quantify this effect, accounting for lithiation-induced material softening, full diffusional-mechanical coupling and plasticity. This map can be used to guide the design of electrodes to improve cyclability and maximize utilizable operational capacity.

## Acknowledgement

Support from the National Research Foundation of Korea through WCU Grant No. R31-2009-000-10083-0 is acknowledged. Y.G. would like to thank Feifei Fan for helpful discussions.

## Appendix A. Two-way coupling between diffusion and stress development

To provide relevant theoretical background, the framework [15,16] for describing the constitutive behavior of the electrode material is briefly summarized here. During charge/discharge, lithium atoms diffuse while the host atoms are assumed to undergo only convection but not diffusion. The elastic strain associated with  $\mathbf{F}^e$  is

$$\boldsymbol{\epsilon}^e \equiv \frac{1}{2} \left( (\mathbf{F}^e)^T (\mathbf{F}^e) - \mathbf{I} \right). \quad (\text{A.1})$$

Since  $\boldsymbol{\epsilon}^e$  is in general small, the elastic stretch  $\mathbf{U}^e$  associated with  $\mathbf{F}^e = \mathbf{R}^e \mathbf{U}^e$  is small, although the rotation  $\mathbf{R}^e$  may be finite. The Cauchy stress  $\boldsymbol{\sigma}$  is given by

$$\sigma_{ij} = F_{ik}^e \left( 3K \epsilon_m^e \delta_{KL} + 2G \epsilon_{KL}^e \right) F_{jL}^e, \quad (\text{A.2})$$

where  $\epsilon_m^e \equiv \epsilon_{kk}^e/3$  and  $\epsilon_{ij}^e \equiv \epsilon_{ij}^e - \epsilon_m^e \delta_{ij}$  are the isotropic and deviatoric parts of the elastic strain;  $K$  and  $G$  are the bulk and shear modulus, respectively.

Plastic deformation is assumed to follow the associated flow rule with a composition-dependent yield surface  $\sigma_Y = \sigma_Y(C^{Li})$  in the form of

$$Q = Q(\boldsymbol{\sigma}) = \frac{1}{2} \boldsymbol{\sigma}^{dev} : \boldsymbol{\sigma}^{dev} - \frac{1}{3} (\sigma_Y)^2 = 0, \quad (\text{A.3})$$

where  $\boldsymbol{\sigma}^{dev} \equiv \boldsymbol{\sigma} - \text{tr}(\boldsymbol{\sigma})/3 \mathbf{I}$  is the deviatoric part of the Cauchy stress. Below the yielding threshold,  $\mathbf{D}$  [Eq. (2)] is simply given by the rate form of Eqs. (3) and (A.2), i.e.

$$\mathbf{D} = \left( \frac{1}{9K} - \frac{1}{6G} \right) \text{tr}(\dot{\boldsymbol{\sigma}}) \mathbf{I} + \frac{\dot{\boldsymbol{\sigma}}}{2G} + \left[ \frac{1}{3} \frac{\partial (\ln J^{SF})}{\partial C^{Li}} \dot{C}^{Li} \right] \mathbf{I}. \quad (\text{A.4})$$

Here,  $\dot{\boldsymbol{\sigma}} \equiv \dot{\boldsymbol{\sigma}} - \mathbf{W} \cdot \boldsymbol{\sigma} + \boldsymbol{\sigma} \cdot \mathbf{W}$  is the objective Jaumann rate of  $\boldsymbol{\sigma}$ , with  $\mathbf{W} = (\mathbf{L} - \mathbf{L}^T)/2$  being the spin tensor. Upon yielding, the rate of deformation including plasticity is

$$\mathbf{D} = \left( \frac{1}{9K} - \frac{1}{6G} \right) \text{tr}(\dot{\boldsymbol{\sigma}}) \mathbf{I} + \frac{\dot{\boldsymbol{\sigma}}}{2G} + \left[ \frac{1}{3} \frac{\partial (\ln J^{SF})}{\partial C^{Li}} \dot{C}^{Li} \right] \mathbf{I} + \dot{\lambda} \frac{\partial Q}{\partial \boldsymbol{\sigma}}, \quad (\text{A.5})$$

where the scalar rate factor  $\dot{\lambda}$  can be determined from consistency conditions and takes the form of

$$\dot{\lambda} = \frac{3}{2} \frac{1}{\sigma_Y^2} \mathbf{D} : \boldsymbol{\sigma}^{dev} + \frac{1}{2G} \frac{\partial \sigma_Y}{\partial C^{Li}} \dot{C}^{Li}. \quad (\text{A.6})$$

Equations (A.5) and (A.6) and give the mechanical constitutive behavior when the yield stress is reached, while Eq. (A.4) governs the deformation in the elastic regime. Together with the conservation of momentum equation

$$\frac{\partial \sigma_{ji}}{\partial x_j} = 0, \quad (\text{A.7})$$

the above equations describe the deformation of the electrode material.

The diffusive flux of lithium can be measured either in the Lagrangian frame as  $\mathbf{J}^{Li}$  or in the updated Lagrangian frame as  $\mathbf{j}^{Li}$ . These measures are related through  $\mathbf{j} \equiv \mathbf{F}^{-1}$  as

$$\mathbf{J}_K^{Li} = \det(\mathbf{F}) f_{Ki} \mathbf{j}_i^{Li}. \quad (\text{A.8})$$

On one hand,  $\mathbf{J}^{Li}$  must satisfy the requirement of mass conservation such that

$$\frac{\partial C^{Li}}{\partial t} + \frac{\partial \mathbf{J}_K^{Li}}{\partial X_K} = R_b^{Li}, \quad (\text{A.9})$$

where  $R_b^{Li}$  is the body source of Li measured in the Lagrangian frame. In this paper, we assume  $R_b^{Li} = 0$ . On the other hand, Fick's law requires

$$\mathbf{J}_K^{Li} = - \frac{D^{Li}}{k_B \theta} f_{Ki} f_{jI} C^{Li} \frac{\partial \mu^{Li}}{\partial X_j}, \quad (\text{A.10})$$

where  $D^{Li} = D^{Li}(\xi)$  is the composition-dependent diffusivity of lithium,  $k_B$  is Boltzmann constant;  $\theta$  is temperature, and  $\mu^{Li}$  is the chemical potential of lithium which can be expressed as

$$\mu^{Li} = \left. \frac{\partial \phi}{\partial C^{Li}} \right|_{\mathbf{F}^e, \theta} - \det(\mathbf{F}^e) \mathcal{Q}^{Li(SF)} \sigma_m. \quad (\text{A.11})$$

Here,  $\sigma_m \equiv \sigma_{kk}/3$  is the hydrostatic stress,  $\mathcal{Q}^{Li(SF)} \equiv \partial J^{SF} / \partial C^{Li}$  is the stress-free partial atomic volume of lithium, and  $\phi = \phi(\mathbf{F}^e, C^{Li}, \theta)$  is the Lagrangian density of the Helmholtz free energy. In this paper, we consider the free energy to be of the form

$$\begin{cases} \phi = \phi^{SF}(C^{Li}, \theta) + w, & \text{where} \\ w \equiv \frac{9}{2} K (\epsilon_m^e)^2 + G \epsilon_{ij}^e \epsilon_{ij}^e = \frac{\sigma_m^2}{2K} + \frac{S_{ij} S_{ij}}{4G}. \end{cases} \quad (\text{A.12})$$

In the above relations,  $\phi^{SF}$  and  $w$  are, respectively, contributions to  $\phi$  due to stress-free chemical interactions and mechanical stresses. Under the assumption that elastic strain  $\boldsymbol{\epsilon}^e$  is small, Eq. (A.11) can be further simplified into

$$\mu^{Li} = \mu_{SF}^{Li} - \det(\mathbf{F}^e) \mathcal{Q}^{Li(SF)} \sigma_m \approx \mu_{SF}^{Li} - \mathcal{Q}^{Li(SF)} \sigma_m. \quad (\text{A.13})$$

Here,

$$\mu_{SF}^{Li} = \partial \phi^{SF} / \partial C^{Li} = \mu_{SF}^{Li}(C^{Li}) \quad (\text{A.14})$$

is the isothermal chemical potential of lithium at zero stress. Generally speaking,  $\mu_{SF}^{Li}(C^{Li})$  can be determined by fitting the activity coefficient to experimentally measured open circuit potential (OCP) data [2]. To simplify the problem, however, we

adopt the ideal-solution form of  $\mu_{SF}^{Li}$  originally proposed by Larche and Cahn [60] and subsequently used by Purkayastha and McMeeking [61] and Yang et al. [62] in the form of

$$\mu_{SF}^{Li} = \mu_*^{Li} + k_B \theta \ln \frac{\xi}{\xi_{\max} - \xi}, \quad (\text{A.15})$$

where  $\xi_{\max}$  is the maximum charge limit of the electrode material and constant  $\mu_*^{Li}$  is a reference chemical potential. The composition-dependent diffusivity  $D^{Li}$ , on the other hand, is taken to be [61]

$$D^{Li} = D_0^{Li} (1 - \Xi). \quad (\text{A.16})$$

$$\left\{ \begin{aligned} \sigma_{Kj}^{PK1} &= \frac{\partial \phi}{\partial F_{jk}} \Big|_{\mathbf{F}^p, C^{Li}, \theta} = \frac{\partial \phi}{\partial F_{jk}^e} \Big|_{C^{Li}, \theta} f_{Kk}^p (V^{SF})^{-1}, \text{ and} \\ \mu^{Li} &= \frac{\partial \phi}{\partial C^{Li}} \Big|_{\mathbf{F}^p, \mathbf{F}, \theta} = \frac{\partial \phi}{\partial C^{Li}} \Big|_{\mathbf{F}^e, \theta} - \frac{\partial \phi}{\partial F_{ij}^e} \Big|_{C^{Li}, \theta} F_{ij}^e \frac{\partial \ln V^{SF}}{\partial C^{Li}} \Big|_{\theta} = \frac{\partial \phi}{\partial C^{Li}} \Big|_{\mathbf{F}^e, \theta} - F_{jk} \sigma_{Kj}^{PK1} \frac{\partial \ln V^{SF}}{\partial C^{Li}}; \end{aligned} \right. \quad (\text{B.5})$$

Here,  $\Xi \equiv \xi / \xi_{\max} = C^{Li} / C_{\max}^{Li}$  is the state-of-charge (SOC), which represents the amount of Li relative to the fully-charged state. Combining Eqs. (A.10–A.16) leads to the following form of the lithium flux,

$$\left. \begin{aligned} J_K^{Li} &= J_K^{Li, chem} + J_K^{Li, mech}, \text{ with} \\ J_K^{Li, chem} &= -D_0^{Li} f_{Kj} \frac{\partial C^{Li}}{\partial X_j} \text{ and} \\ J_K^{Li, mech} &= \frac{D_0^{Li} (1 - \Xi)}{k_B \theta} f_{Kj} C^{Li} \frac{\partial [\Omega^{Li(SF)} \sigma_m]}{\partial X_j}. \end{aligned} \right\} \quad (\text{A.17})$$

In the above relations,  $J_K^{Li, chem}$  and  $J_K^{Li, mech}$  are contributions due to chemical interaction and mechanical driving force, respectively. According to Purkayastha and McMeeking [61], the main advantage of Eqs. (A.15) and (A.16) is that it correctly captures the fact that the stress-gradient-driven diffusion flux  $J_K^{Li, mech}$  [cf. Eq. (A.17)] vanishes at the charging limits of  $\xi = 0$  and  $\xi = \xi_{\max}$ .

A mixed finite element framework [29,30] is used to analyze the coupled diffusion/deformation processes delineated by Eqs. (A.3)–(A.17). Details of this numerical framework are given in [29].

## Appendix B. Proof of equation (24)

$J^*(\Gamma)$  as defined in Eq. (23) is path-dependent and equals to

$$J^*(\partial \Omega) = - \int_{\partial \Omega} w^p \delta_{1j} N_j d\Gamma_0 + \int_{\Omega} \mu^{Li} \frac{\partial C^{Li}}{\partial X_1} dA_0 \quad (\text{B.1})$$

for any continuum domain  $\Omega$  bound by boundary  $\Gamma = \partial \Omega$ . To demonstrate this, we first note that balance of momentum [Eq. (A.7)] requires that

$$\frac{\partial \sigma_{ji}^{PK1}}{\partial X_j} = 0. \quad (\text{B.2})$$

Therefore, invoking the divergence theorem on Eq. (23) leads to

$$J^*(\partial \Omega) = \int_{\Omega} \left[ \frac{\partial \phi}{\partial X_1} - \sigma_{ji}^{PK1} \frac{\partial F_{ij}}{\partial X_1} \right] dA_0. \quad (\text{B.3})$$

The Lee decomposition [Eq. (1)] indicates that

$$\frac{\partial F_{ij}}{\partial X_1} = \frac{\partial F_{ij}^e}{\partial X_1} V^{SF} F_{ij}^p + F_{ij}^e V^{SF} \frac{\partial F_{ij}^p}{\partial X_1} + F_{ij} \frac{\partial \ln V^{SF}}{\partial X_1}. \quad (\text{B.4})$$

For free energy of the form  $\phi = \phi(\mathbf{F}^e, C^{Li}, \theta)$ , the 1<sup>st</sup> Piola-Kirchhoff stress and Li chemical potential are, respectively,

where  $\mathbf{f}^p = (\mathbf{F}^p)^{-1}$ . Therefore, under isothermal conditions,

$$\begin{aligned} \frac{\partial \phi}{\partial X_1} &= \frac{\partial \phi}{\partial F_{ij}^e} \Big|_{C^{Li}} \frac{\partial F_{ij}}{\partial X_1} + \frac{\partial \phi}{\partial C^{Li}} \Big|_{\mathbf{F}^e} \frac{\partial C^{Li}}{\partial X_1} \\ &= V^{SF} F_{jk}^p \sigma_{Kj}^{PK1} \frac{\partial F_{ij}^e}{\partial X_1} + \left( \mu^{Li} + F_{jk} \sigma_{Kj}^{PK1} \frac{\partial \ln V^{SF}}{\partial C^{Li}} \right) \frac{\partial C^{Li}}{\partial X_1}. \\ &= V^{SF} F_{jk}^p \sigma_{Kj}^{PK1} \frac{\partial F_{ij}^e}{\partial X_1} + \mu^{Li} \frac{\partial C^{Li}}{\partial X_1} + F_{jk} \sigma_{Kj}^{PK1} \frac{\partial \ln V^{SF}}{\partial X_1} \end{aligned} \quad (\text{B.6})$$

In the derivation of Eq. (B.6), it is assumed that  $V^{SF}$  is uniquely determined by current Li concentration [Eq. (3)].

Combining Eqs. (B.4) and (B.6) leads to

$$\frac{\partial \phi}{\partial X_1} - \sigma_{ji}^{PK1} \frac{\partial F_{ij}}{\partial X_1} = \mu^{Li} \frac{\partial C^{Li}}{\partial X_1} - \sigma_{ji}^{PK1} F_{ij}^e V^{SF} \frac{\partial F_{ij}^p}{\partial X_1}. \quad (\text{B.7})$$

With the assumption that elastic strains are small (i.e.,  $F_{ij}^e F_{ij}^p \approx \delta_{ij}$ ), the second term on the right hand side of Eq. (B.7) can be easily transformed into

$$\sigma_{ji}^{PK1} F_{ij}^e V^{SF} \frac{\partial F_{ij}^p}{\partial X_1} \approx (V^{SF})^2 \sigma_{jk}^{PK2} \frac{\partial E_{jk}^p}{\partial X_1}, \quad (\text{B.8})$$

where the plastic strain is defined as  $E_{jk}^p \equiv \frac{1}{2} (F_{ij}^p F_{jk}^p - \delta_{ij})$ . By Eqs. (B.3), (B.7) and (B.8), one obtains

$$J^*(\partial \Omega) = \int_{\Omega} \mu^{Li} \frac{\partial C^{Li}}{\partial X_1} dA_0 - \int_{\Omega} (V^{SF})^2 \sigma_{jk}^{PK2} \frac{\partial E_{jk}^p}{\partial X_1} dA_0. \quad (\text{B.9})$$

To proceed further, we define the plastic work as

$$w^p \equiv \int_0^t \det(\mathbf{F}) \boldsymbol{\sigma} : \mathbf{D}^p dt \approx \int_0^t (V^{SF})^2 \sigma_{jk}^{PK2} \dot{E}_{jk}^p dt \quad (\text{B.10})$$

and adopt the standard approximation such that

$$\frac{\partial w^P}{\partial X_1} \approx (V^{SF})^2 \sigma_{JK}^{PK2} \frac{\partial E_{JK}^P}{\partial X_1}. \quad (\text{B.11})$$

Substitution of Eq. (B.11) into Eq. (B.9) and the divergence theorem lead to

$$J^*(\partial\Omega) = \int_{\Omega} \mu^{Li} \frac{\partial C^{Li}}{\partial X_1} dA_0 - \int_{\partial\Omega} w^P \delta_{1j} N_j d\Gamma_0. \quad (\text{B.12})$$

The validity of Eq. (B.12) mostly depends on how significant the error associated with approximation (B.11) is. The path independency of Eq. (30) is therefore less reliable when approximation (B.11) breaks down. Indeed, for cracks in elasto-plastic materials, contours that are very close to the crack tip should not be used.

### Appendix C. Implementation of $J$ using the energy domain integral method

Equation (30) is the path-independent form of the energy release rate used in this paper for the numerical evaluation of  $G$ . To facilitate numerical calculation, note that Eq. (A.11)–(A.13) allow Eq. (26) to be further simplified into

$$J = J(\Gamma) = \int_{\Gamma} \left[ (w + w^P) \delta_{1j} - \sigma_{ji}^{PK1} (\partial u_i / \partial X_1) \right] N_j d\Gamma_0 - \int_{V_r} \left( \frac{\partial w}{\partial C^{Li}} \Big|_{\mathbf{F}^e, \theta} - \det(\mathbf{F}^e) \Omega^{Li(SF)} \sigma_m \right) \frac{\partial C^{Li}}{\partial X_1} dA_0, \quad (\text{C.1})$$

which consists of a contour integral over a finite path and an area integral over a finite domain.

Based on Eq. (C.1), we adopt the method originally proposed by Shih et al. [40] in order to facilitate the computation of  $J(\Gamma)$ . For arbitrary contours  $\Gamma$  and  $C_0$  (cf. Fig. 1), consider a sufficiently smooth field of  $q^* = q^*(\mathbf{X})$  such that  $q^* = 1$  on  $\Gamma$  and  $q^* = 0$  on  $C_0$ . Here,  $\Gamma$  is not necessarily infinitesimal. For traction-free crack surfaces  $C_-$  and  $C_+$ , the path-independent expression of energy release rate [Eq. (C.1)] can be rewritten as

$$J = J(\Gamma) = \int_{C_- + C_0 + C_+ - \Gamma} \left[ - (w + w^P) \delta_{1j} + \sigma_{ji}^{PK1} (\partial u_i / \partial X_1) \right] q^* N_j d\Gamma_0 - \int_{V_r} \left( \frac{\partial w}{\partial C^{Li}} \Big|_{\mathbf{F}^e, \theta} - \det(\mathbf{F}^e) \Omega^{Li(SF)} \sigma_m \right) \frac{\partial C^{Li}}{\partial X_1} dA_0. \quad (\text{C.2})$$

Here,  $-\Gamma$  stands for contour  $\Gamma$  with the opposite loop direction. Application of the divergence theorem leads to

$$\begin{cases} J = J(\Gamma) = \int_A q^* \left[ - \frac{\partial (w + w^P)}{\partial X_1} + \sigma_{ji}^{PK1} \frac{\partial F_{ij}}{\partial X_1} \right] dA_0 \\ + \int_A \frac{\partial q^*}{\partial X_j} \left[ - (w + w^P) \delta_{1j} + \sigma_{ji}^{PK1} \frac{\partial u_i}{\partial X_1} \right] dA_0 \\ - \int_{V_r} \left( \frac{\partial w}{\partial C^{Li}} \Big|_{\mathbf{F}^e, \theta} - \det(\mathbf{F}^e) \Omega^{Li(SF)} \sigma_m \right) \frac{\partial C^{Li}}{\partial X_1} dA_0. \end{cases} \quad (\text{C.3})$$

With Eqs. (A.11)–(A.13) and (C.3),

$$\begin{cases} J = \int_A \frac{\partial q^*}{\partial X_j} \left[ \sigma_{ji}^{PK1} \frac{\partial u_i}{\partial X_1} - (w + w^P) \delta_{1j} \right] dA_0 \\ + \int_{V_r} \left[ \det(\mathbf{F}^e) \Omega^{Li(SF)} \sigma_m - \frac{\partial w}{\partial C^{Li}} \Big|_{\mathbf{F}^e, \theta} \right] \frac{\partial C^{Li}}{\partial X_1} dA_0 \\ + \int_A q^* \left[ \det(\mathbf{F}^e) \Omega^{Li(SF)} \sigma_m - \frac{\partial w}{\partial C^{Li}} \Big|_{\mathbf{F}^e, \theta} \right] \frac{\partial C^{Li}}{\partial X_1} dA_0. \end{cases} \quad (\text{C.4})$$

Here,  $\Gamma$  and  $C_0$  are arbitrary (cf. Fig. 1a) and  $\Gamma$  is not necessarily infinitesimal.

### Appendix D. The path independency of $J$ and associated numerical error

The accuracy of the path-independent expressions of  $J$  [Eqs. (30) and (31)] is contingent upon the accuracy of the approximation in Eq. (B.11). To validate this approximation, we consider two integration paths as shown in Fig. D.1(b). The material parameters and system dimensions are the same as those used for Fig. 9, with  $\bar{\sigma}_Y = 0.01$ .

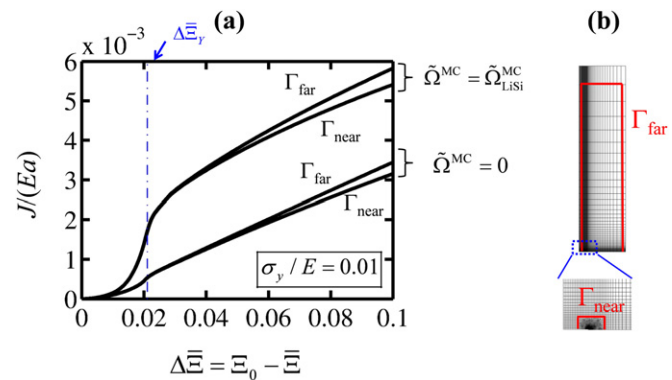


**Fig. D.1.** Path independency of  $J$ . (a)  $J$  calculated for two different contour paths,  $\Gamma_{near}$  and  $\Gamma_{far}$ . (b) Location of  $\Gamma_{near}$  and  $\Gamma_{far}$ . The material parameters and system configuration are the same as those for Fig. 9 in the main text, with  $\bar{\sigma}_Y = 0.01$ .

Up to the point of  $\Delta \bar{\Xi}_Y$ ,  $J^{CP}(\Gamma^{far})$  and  $J^{CP}(\Gamma^{near})$  [and also  $J^{NCP}(\Gamma^{far})$  and  $J^{NCP}(\Gamma^{near})$ ] calculated for the two paths shown in Fig. D.1(b) differ by less than 0.5%. However, this error begins to increase once the film yields globally. This divergence is intrinsic to all calculations of  $J$ -integral and is not specific to the diffusion-deformation two-way coupled problems considered here. Even for purely mechanical cases,  $J$  calculated for different paths do not show good asymptotic behavior when  $\Gamma \rightarrow 0$ . Instead,  $J$  converges to the same value of  $J^\infty$  when  $\Gamma \rightarrow \infty$  [63]. Therefore, although by definition per se the energy release rate is given with  $\Gamma \rightarrow 0$  [Eq. (20)], computations should be performed on  $\Gamma$  that is as far as possible from the crack tip. We therefore perform all our calculations for  $J$  using the largest possible contour. For all calculations involved in this paper,  $J^{CP}(\Gamma^{far})$  and  $J^{CP}(\Gamma^{near})$  never differ by more than 10%.

### References

- [1] L.Y. Beaulieu, K.W. Eberman, R.L. Turner, L.J. Krause, J.R. Dahn, Electrochemical and Solid State Letters 4 (2001) A137–A140.
- [2] J. Christensen, J. Newman, Journal of Solid State Electrochemistry 10 (2006) 293–319.



- [3] C.K. Chan, H.L. Peng, G. Liu, K. McIlwrath, X.F. Zhang, R.A. Huggins, Y. Cui, *Nature Nanotechnology* 3 (2008) 31–35.
- [4] L.F. Cui, R. Ruffo, C.K. Chan, H.L. Peng, Y. Cui, *Nano Letters* 9 (2009) 491–495.
- [5] T. Song, J.L. Xia, J.H. Lee, D.H. Lee, M.S. Kwon, J.M. Choi, J. Wu, S.K. Doo, H. Chang, W. Il Park, D.S. Zang, H. Kim, Y.G. Huang, K.C. Hwang, J.A. Rogers, U. Paik, *Nano Letters* 10 (2010) 1710–1716.
- [6] A. Magasinski, P. Dixon, B. Hertzberg, A. Kvit, J. Ayala, G. Yushin, *Nature Materials* 9 (2010) 353–358.
- [7] L.B. Hu, H. Wu, Y.F. Gao, A.Y. Cao, H.B. Li, J. McDough, X. Xie, M. Zhou, Y. Cui, *Advanced Energy Materials* 1 (2011) 523–527.
- [8] H. Haftbaradaran, H.J. Gao, W.A. Curtin, *Applied Physics Letters* 96 (2010) 091909.
- [9] Y.T. Cheng, M.W. Verbrugge, *Journal of Applied Physics* 104 (2008) 083521.
- [10] X. Zhang, W. Shyy, A. Marie Sastry, *Journal of the Electrochemical Society* 154 (2007) A910.
- [11] I. Ryu, J.W. Choi, Y. Cui, W.D. Nix, *Journal of the Mechanics and Physics of Solids* 59 (2011) 1717–1730.
- [12] Z.W. Cui, F. Gao, J.M. Qu, *Journal of the Mechanics and Physics of Solids* 60 (2012) 1280–1295.
- [13] K.J. Zhao, M. Pharr, Q. Wan, W.L. Wang, E. Kaxiras, J.J. Vlassak, Z.G. Suo, *Journal of the Electrochemical Society* 159 (2012) A238–A243.
- [14] R.T. Purkayastha, R.M. McMeeking, *Computational Mechanics* 50 (2012) 209–227.
- [15] A.F. Bower, P.R. Guduru, V.A. Sethuraman, *Journal of the Mechanics and Physics of Solids* 59 (2011) 804–828.
- [16] Y.F. Gao, M. Zhou, *Journal of Applied Physics* 109 (2011) 014310.
- [17] Y.F. Gao, M. Zhou, *Acta Mechanica Sinica* 28 (2012) 1068–1077.
- [18] R. Deshpande, Y.T. Cheng, M.W. Verbrugge, *Journal of Power Sources* 195 (2010) 5081–5088.
- [19] K.J. Zhao, M. Pharr, S.Q. Cai, J.J. Vlassak, Z.G. Suo, *Journal of the American Ceramic Society* 94 (2011) S226–S235.
- [20] V.A. Sethuraman, N. Van Winkle, D.P. Abraham, A.F. Bower, P.R. Guduru, *Journal of Power Sources* 206 (2012) 334–342.
- [21] K.J. Zhao, W.L. Wang, J. Gregoire, M. Pharr, Z.G. Suo, J.J. Vlassak, E. Kaxiras, *Nano Letters* 11 (2011) 2962–2967.
- [22] B. Hertzberg, J. Benson, G. Yushin, *Electrochemistry Communications* 13 (2011) 818–821.
- [23] V.B. Shenoy, P. Johari, Y. Qi, *Journal of Power Sources* 195 (2010) 6825–6830.
- [24] Z.W. Cui, F. Gao, Z.H. Cui, J.M. Qu, *Journal of Power Sources* 207 (2012) 150–159.
- [25] M. Tang, W.C. Carter, J.F. Belak, Y.M. Chiang, *Electrochimica Acta* 56 (2010) 969–976.
- [26] M. Tang, H.Y. Huang, N. Meethong, Y.H. Kao, W.C. Carter, Y.M. Chiang, *Chemistry of Materials* 21 (2009) 1557–1571.
- [27] P. Sofronis, J. Lufrano, *Materials Science and Engineering A-Structural Materials Properties Microstructure and Processing* 260 (1999) 41–47.
- [28] R. Grantab, V.B. Shenoy, *Journal of the Electrochemical Society* 159 (2012) A584–A591.
- [29] Y.F. Gao, M. Cho, M. Zhou, *Journal of the Mechanics and Physics of Solids* 61 (2013) 579–596.
- [30] A.F. Bower, P.R. Guduru, *Modelling and Simulation in Materials Science and Engineering* 20 (2012) 045004.
- [31] X.H. Chen, *International Journal of Fracture* 148 (2007) 47–55.
- [32] M. Zhou, G. Ravichandran, A.J. Rosakis, *Journal of the Mechanics and Physics of Solids* 44 (1996) 1007.
- [33] T. Nakamura, C.F. Shih, L.B. Freund, *International Journal of Fracture* 27 (1985) 229–243.
- [34] Y. Li, M. Zhou, *Journal of the Mechanics and Physics of Solids* 61 (2013) 472–488.
- [35] E.H. Lee, *Journal of Applied Mechanics* 36 (1969) 1.
- [36] D.K. Kondepudi, I. Prigogine, *Modern Thermodynamics: From Heat Engines to Dissipative Structures*, John Wiley, Chichester, New York, 1998.
- [37] B. Moran, C.F. Shih, *Engineering Fracture Mechanics* 27 (1987) 615–642.
- [38] B. Moran, C.F. Shih, *International Journal of Fracture* 35 (1987) 295–310.
- [39] L.B. Freund, *Dynamic Fracture Mechanics*, Cambridge University Press, Cambridge, New York, 1990.
- [40] C.F. Shih, B. Moran, T. Nakamura, *International Journal of Fracture* 30 (1986) 79–102.
- [41] M. Szabadi, P. Hess, A.J. Kellock, H. Coufal, J.E.E. Baglin, *Physical Review B* 58 (1998) 8941–8948.
- [42] T.K. Bhandakkar, H.J. Gao, *International Journal of Solids and Structures* 47 (2010) 1424–1434.
- [43] N. Ding, J. Xu, Y.X. Yao, G. Wegner, X. Fang, C.H. Chen, I. Lieberwirth, *Solid State Ionics* 180 (2009) 222–225.
- [44] E.M. Pell, *Physical Review* 119 (1960) 1014–1021.
- [45] R. Ruffo, S.S. Hong, C.K. Chan, R.A. Huggins, Y. Cui, *Journal of Physical Chemistry C* 113 (2009) 11390–11398.
- [46] J. Xie, N. Imanishi, T. Zhang, A. Hirano, Y. Takeda, O. Yamamoto, *Materials Chemistry and Physics* 120 (2010) 421–425.
- [47] P. Johari, Y. Qi, V.B. Shenoy, *Nano Letters* 11 (2011) 5494–5500.
- [48] M.N. Obrovac, L. Christensen, *Electrochemical and Solid State Letters* 7 (2004) A93–A96.
- [49] A.H. Heuer, F.F. Lange, M.V. Swain, A.G. Evans, *Journal of the American Ceramic Society* 69 (1986) R1–R4.
- [50] Y.T. Cheng, M.W. Verbrugge, *Journal of the Electrochemical Society* 157 (2010) A508–A516.
- [51] K.J. Zhao, M. Pharr, J.J. Vlassak, Z.G. Suo, *Journal of Applied Physics* 108 (2010) 073517.
- [52] S.K. Soni, B.W. Sheldon, X.C. Xiao, M.W. Verbrugge, D. Ahn, H. Haftbaradaran, H.J. Gao, *Journal of the Electrochemical Society* 159 (2012) A38–A43.
- [53] H. Haftbaradaran, X.C. Xiao, M.W. Verbrugge, H.J. Gao, *Journal of Power Sources* 206 (2012) 357–366.
- [54] J.C. Li, X.C. Xiao, F.Q. Yang, M.W. Verbrugge, Y.T. Cheng, *Journal of Physical Chemistry C* 116 (2012) 1472–1478.
- [55] T.L. Anderson, *Fracture Mechanics: Fundamentals and Applications*, third ed., Taylor & Francis, Boca Raton, FL, 2005.
- [56] S. Aoki, K. Kishimoto, M. Sakata, *Engineering Fracture Mechanics* 16 (1982) 405–413.
- [57] M. Chon, V. Sethuraman, A. McCormick, V. Srinivasan, P. Guduru, *Physical Review Letters* 107 (2011).
- [58] V. Sethuraman, M. Chon, M. Shimshak, V. Srinivasan, P. Guduru, *Journal of Power Sources* 195 (2010) 5062–5066.
- [59] R.F. Cook, *Journal of Materials Science* 41 (2006) 841–872.
- [60] F.C. Larche, J.W. Cahn, *Acta Metallurgica* 33 (1985) 331–357.
- [61] R. Purkayastha, R.M. McMeeking, *Journal of Applied Mechanics-Transactions of the ASME* 79 (2012) 031021.
- [62] B. Yang, Y.P. He, J. Irsa, C.A. Lundgren, J.B. Ratchford, Y.P. Zhao, *Journal of Power Sources* 204 (2012) 168–176.
- [63] D. Carka, R.M. McMeeking, C.M. Landis, *Journal of Applied Mechanics-Transactions of the ASME* 79 (2012) 044502.

## Nomenclature

- $a$ : Crack length [m]  
 $c^H, c^{Li}$ : Eulerian concentration of host (H) and lithium (Li) [atoms  $m^{-3}$ ]  
 $C^H, C^{Li}$ : Lagrangian concentration of host (H) and lithium (Li) [atoms  $m^{-3}$ ]  
 $d^{crack}$ : Nominal out-of-plane thickness of the 2-D cracked system [m]  
 $\mathbf{D}, \mathbf{D}^e, \mathbf{D}^{SF}, \mathbf{D}^p$ : Total, elastic, stress-free volumetric and plastic rates of deformation [ $s^{-1}$ ]  
 $D^{Li}$ : Concentration-dependent diffusivity of Li [ $m^2 s^{-1}$ ]  
 $D_0^{Li}$ : Characteristic concentration-independent diffusivity of Li [ $m^2 s^{-1}$ ]  
 $e$ : Internal energy per unit reference volume [J  $m^{-3}$ ]  
 $E$ : Young's modulus [Pa]  
 $\mathbf{F}, \mathbf{F}^e, \mathbf{F}^{SF}, \mathbf{F}^p$ : Total, elastic, stress-free volumetric and plastic deformation gradients  
 $G$ : Shear modulus [Pa]  
 $J$ : Energy release rate for fracture [J  $m^{-2}$ ]  
 $J_{CR}$ : Critical energy release rate for fracture [J  $m^{-2}$ ]  
 $J^{SF}$ : Volume change due to changes in Li concentration [ $J^{SF} \equiv \det(\mathbf{F}^{SF})$ ]  
 $\mathbf{J}^L$ : Lagrangian flux of lithium [atoms  $m^{-2} s^{-1}$ ]  
 $\mathbf{J}^q$ : Lagrangian flux of heat [J  $m^{-2} s^{-1}$ ]  
 $\mathbf{J}^s$ : Lagrangian flux of entropy [J  $K^{-1} m^{-2} s^{-1}$ ]  
 $K$ : Bulk modulus [Pa]  
 $K_I$ : Mode-I stress intensity factor [ $Pa m^{1/2}$ ]  
 $K_{IC}$ : Plane strain fracture toughness [ $Pa m^{1/2}$ ]  
 $l$ : Crack length measured in Lagrangian configuration [m]  
 $n^{Li}$ : Amount of Li in the crack system per unit  $d^{crack}$  [atoms  $m^{-1}$ ]  
 $S^{crack}$ : Entropy of crack subsystem per unit  $d^{crack}$  [J  $K^{-1} m^{-1}$ ]  
 $T_0$ : Characteristic loading time [s]  
 $U^{crack}$ : Internal energy of crack subsystem per unit  $d^{crack}$  [J  $m^{-1}$ ]  
 $u^{Li}$ : Partial internal energy of Li [J per atom]  
 $v$ : Velocity of material point [m  $s^{-1}$ ]  
 $V^{SF}$ : Isotropic stretch due to changes in Li concentration [ $V^{SF} \equiv (J^{SF})^{1/3}$ ]  
 $w$ : Elastic energy per unit Lagrangian volume [J  $m^{-3}$ ]  
 $w^p$ : Plastic potential [J  $m^{-3}$ ]  
 $\mathbf{x}$ : Position of material point in current configuration [m]  
 $\mathbf{X}$ : Position of material point in reference configuration [m]
- Greek*  
 $\gamma$ : Surface energy per unit crack area [J  $m^{-2}$ ]  
 $\epsilon^e$ : Elastic strain  
 $\epsilon_{eff}^p$ : Effective plastic strain  
 $\eta$ : Entropy per unit reference volume [J  $K^{-1} m^{-3}$ ]  
 $\theta$ : Temperature in the continuum [K]  
 $\theta^{crack}$ : Temperature in the crack subsystem [K]  
 $\mu^{Li}$ : Chemical potential of Li in the continuum [J per atom]  
 $\mu^{Li,crack}$ : Chemical potential of Li in the crack subsystem [J per atom]  
 $\mu_*^{Li}$ : Reference chemical potential of Li [J per atom]  
 $\nu$ : Poisson's ratio  
 $\xi$ : Lithium number per host in chemical formula  $Li_\xi H$   
 $\xi_{max}$ : Maximum  $\xi$  at the fully charged state  
 $\bar{E}$ : State of charge (SOC) [ $\bar{E} \equiv \xi/\xi_{max}$ ]  
 $\bar{E}_0$ : Initial SOC  
 $\bar{E}$ : Domain-average SOC  
 $\Delta \bar{E}$ : Dimensionless discharge level  
 $\Delta \bar{E}_Y$ : Discharge level at which thin film begins to yield globally  
 $\Delta \bar{E}_{CR}$ : Critical discharge level at which  $J = J_{CR}$   
 $\sigma$ : Cauchy stress [Pa]  
 $\sigma_m, \sigma_{mises}$ : Hydrostatic and von Mises invariants of Cauchy stress [Pa]  
 $\sigma^{PK1}, \sigma^{PK2}$ : First and second Piola–Kirchhoff stresses [Pa]

$\sigma_Y$ : Yield stress [Pa]

$\bar{\sigma}_Y$ : Dimensionless yield stress [ $\bar{\sigma}_Y \equiv \sigma_Y/E$ ]

$\sigma_\infty$ : Remote stress [Pa]

$\Sigma$ : Entropy production rate per unit reference volume [ $\text{J K}^{-1} \text{m}^{-3} \text{s}^{-1}$ ]

$\Sigma^P, \Sigma^{NP}$ : Plastic and non-plastic contributions to  $\Sigma$  [ $\text{J K}^{-1} \text{m}^{-3} \text{s}^{-1}$ ]

$\phi$ : Helmholtz free energy per unit Lagrangian volume [ $\text{J m}^{-3}$ ]

$\phi^{crack}$ : Helmholtz free energy of crack subsystem per unit  $d^{crack}$  [ $\text{J m}^{-1}$ ]

$\mathcal{Q}^{\text{Li(SF)}}$ : Partial atomic volume of Li [ $\text{m}^3$  per atom]

$\bar{\mathcal{Q}}^{\text{CM}}, \bar{\mathcal{Q}}^{\text{MC}}$ : Chemical-to-mechanical and mechanical-to-chemical dimensionless partial atomic volumes

*Subscript/Superscript*

CP: Pertaining to full deformation–diffusion coupling

eff: Effective value

NCP: Pertaining to situations with  $\bar{\mathcal{Q}}^{\text{MC}} = 0$